Supplementary Information

Low-Voltage Syngas Synthesis via BPM Electrolysis of CO_2 Capture and Aldehyde Solution

Po-Wei Huang[1]†, Hyeonuk Choi[2]†, Anush Venkataraman[1], Olivia Vulpin[3], Claudio A. Ruiz Torres[4], Danae A. Chipoco Haro[5], Yaguang Zhu[4], Erika R. Yamazaki[1], Kelsey B. Hatzell[4], Shannon W. Boettcher[3,6,7], Sankar Nair[1], Jihun Oh[2]*, Hakhyeon Song[8]*, Marta C. Hatzell[1,8]*

Affiliations:

[1]School of Chemical and Biomolecular Engineering, Georgia Institute of Technology, Atlanta, GA 30332, USA.
[2]Department of Materials Science and Engineering, Korea Advanced Institute of Science and Technology (KAIST), Daejeon 34141, Republic of Korea.
[3]Department of Chemistry and Biochemistry, Oregon Center for Electrochemistry, University of Oregon, Eugene, Oregon 97403, United States.
[4]Andlinger Center for Energy and the Environment, Princeton University, Princeton, New Jersey 08540, United States.
[5]School of Materials Science and Engineering, Georgia Institute of Technology, Atlanta, Georgia 30332, United States.
[6]Department of Chemical & Biomolecular Engineering and Department of Chemistry, University of California, Berkeley, California 94720, United States
[7]Energy Storage and Distributed Resources Division, Lawrence Berkeley National Laboratory, Berkeley, California 94720, United States
[8]George W. Woodruff School of Mechanical Engineering, Georgia Institute of Technology, Atlanta, Georgia 30332, United States.

***Corresponding author. Email: jihun.oh@kaist.ac.kr (J. O.); hakhyeon.song@me.gatech.edu (H. S.) marta.hatzell@me.gatech.edu (M. C. H.)**
†These authors contributed equally to this work.

Materials and Methods

Synthesis of Cu-based electrodes

The synthesis procedure for Cu/Cu_2O was adapted from a previously reported method.[1] Commercial Cu foam (1 × 2 cm^2, MSE Supplies) was sequentially cleaned with ethanol and deionized (DI) water, followed by immersion in 2 M HCl solution (ACS reagent, Sigma-Aldrich) for 5 min to remove native oxide layers from the surface. The cleaned Cu foam was immersed in 100 mL of aqueous solution containing 10.7 g of sodium hydroxide (≥97.0%, ACS reagent, Sigma-Aldrich) and 3 g of ammonium persulfate [$(NH_4)_2S_2O_8$, ≥98%, ACS reagent, Sigma-Aldrich] at room temperature for 30 min to induce the growth of $Cu(OH)_2$ nanorods on its surface. The resulting $Cu(OH)_2$-coated Cu foam was thoroughly washed with DI water and ethanol, dried under nitrogen flow, and calcined at 550 °C for 3 h under argon atmosphere (1000 mL min^{-1}) with a ramp rate of 1 °C min^{-1} to form Cu_2O-coated Cu foam. The Cu_2O-coated Cu foam was then subjected to electrochemical reduction at −1.4 V versus Hg/HgO (1 M NaOH) for 400 s in 1 M KOH (≥85%, ACS reagent, Sigma-Aldrich) to partially convert Cu_2O into metallic Cu, thereby forming a mixed-phase Cu/Cu_2O structure. To prepare the Cu electrode, pristine Cu foam was pretreated at −1.4 V vs. Hg/HgO (1 M NaOH) in 1 M KOH for 400 s, ensuring complete reduction of native surface oxides to metallic Cu. The Cu_2O electrode was prepared using the same procedure as the Cu/Cu_2O electrode, with the key difference being that it was not electrochemically reduced but instead used directly after calcination. To prepare the CuO electrode, pristine Cu foam was calcined at 550 °C for 3 h in air with a ramp rate of 1 °C min^{-1} and used directly after calcination

Synthesis of pulse-treated Cu foam

Pulse-treated Cu foam was prepared through a two-step electrochemical process. First, pristine Cu foam was pretreated at −1.4 V vs. Hg/HgO (1 M NaOH) in 1 M KOH for 400 s to fully reduce native surface oxides to metallic Cu. Following this pretreatment, a pulsed potential protocol was applied using fixed anodic (E_a = −0.38 V) and cathodic (E_c = −1.4 V) potential vs. Hg/HgO. The anodic and cathodic pulse durations were set to 15 s and 0.5 s, respectively. This sequence was repeated for 100 cycles.

Synthesis of Ni single atom catalyst (Ni-SAC)

To prepare Ni-SAC, 48 g of nickel(II) nitrate hexahydrate ($Ni(NO_3)_2 \cdot 6H_2O$, ACS reagent, Supelco), 216 g of 2-methylimidazole (99%, Sigma-Aldrich), and 80 g of carbon black (Vulcan XC 72R, Fuel Cell Store) were dispersed in 2.5 L of ethanol in a 3 L glass vessel. The suspension was ultrasonicated for 1 h to ensure uniform dispersion of the precursors. Ethanol was subsequently removed using rotary evaporation at 65 °C under vacuum, with the rotation speed set at 250 rpm. The resulting solid was dried and finely ground using an agate mortar and pestle to obtain a homogeneous precursor powder. Cal cination was carried out at 800 °C for 2 h under constant argon flow of 3 L min^{-1} in an atmosphere box furnace, with a temperature ramp rate of 1 °C min^{-1}. After cooling to room temperature, the calcined material was subjected to ball milling using 10 mm yttria-stabilized zirconia balls to obtain the final Ni-SAC powder. The total yield of the catalyst was 105.12 g.

Ni-SAC Electrode Preparation

The Ni-SAC electrode was prepared using a spray-coating method. A catalyst ink consisting of 40 mg of Ni-SAC powder, 48.2 µL of PFSA dispersion (D5, 5%, alcohol-based, Fuel Cell Store), and 5 mL of ethanol was ultrasonicated for at least 1 h to ensure uniform dispersion. Hydrophilic carbon paper (AvCarb MGL 190, Fuel Cell Store) was pre-dried on a hot plate at 150 °C. The catalyst ink was then applied to the carbon paper using an airbrush system (Master Airbrush) until a target loading of 2 mg cm^{-2} was achieved. The final catalyst loading was determined by measuring the electrode mass before and after spray coating.

Bipolar Membrane Synthesis

The anion-exchange membrane (PAP-TP-85, Versogen) was conditioned by removing its plastic backing and immersing it in a 1 M KOH solution. The KOH bath was refreshed after 24 hours, and the membrane was stored in 1 M KOH until use. The cation-exchange membrane was prepared by dissolving sulfonated poly(ether ether ketone) (SPEEK) powder in dimethylacetamide (DMAc) at a SPEEK-to-DMAc weight ratio of 25 wt%. The solution was allowed to stand at room temperature (RT) for at least 48 hours to ensure complete mixing. SnO_2 catalyst synthesis followed the protocol reported by Sasmal et al..[2] Starting with $SnCl_4 \cdot 5\ H_2O$ (Sigma Aldrich), a 0.05 M solution in deionized water is dissolved at RT in a round bottom flask. This solution is then refluxed in a bath at 90–95 °C for 20 min. The solution appeared milky white and was allowed to

cool for 30 min before being transferred to 50 mL centrifuge tubes. The tubes were filled to 50 mL with deionized water and centrifuged at 7000 rpm for 5 min. The supernatant was discarded and replaced with deionized water, followed by centrifugation. This washing step was repeated five times. The resulting SnO_2 paste was then dispersed in a 1:1 (v/v) mixture of isopropanol and water to prepare a 2 wt% suspension. The 2 wt% SnO_2 suspension was either spin-coated directly onto the Versogen membrane or diluted and applied via spray coating. After catalyst deposition, the SPEEK/DMAc solution was cast over the membrane using a 130 μm doctor blade. The coated membrane was baked in a vented oven at 60 ^{o}C overnight to evaporate DMAc, then hydrated in deionized water for at least 48 hours prior to testing.

Materials Characterization

The morphology and surface structure of the samples were characterized using scanning electron microscopy (SEM, JSM-IT800, JEOL Ltd., Japan and Hitachi SU8230). Elemental distribution mapping was analyzed via energy-dispersive X-ray spectroscopy (EDS) equipped with an Xflash Detector 6-60 (Bruker, Germany). Atomic-scale structure and compositional analyses were conducted using high-angle annular dark-field scanning transmission electron microscopy (HAADF-STEM) coupled with EDS mapping (Titan Cubed G2 60–300, FEI Company, USA) operated at an accelerating voltage of 200 kV at the KARA (KAIST Analysis center for Research Advancement). Surface chemical states and elemental compositions were examined using X-ray photoelectron spectroscopy (XPS; Sigma Probe, Thermo VG Scientific, USA, and Thermo K-Alpha), equipped with a monochromatic Al Kα X-ray source (hν = 1486.7 eV) and Ar ion sputtering. The binding energies were calibrated to the C 1s peak at 284.8 eV to account for surface charging. Crystalline phases were identified using X-ray diffraction (XRD, SmartLab, Rigaku, Japan) with Cu $K\alpha_1$ radiation (λ = 1.5406 Å). Phase identification was performed by matching the obtained patterns with standard reference data. Quantitative phase analysis was conducted using the Reference Intensity Ratio (RIR) method in PDXL software (Rigaku, Japan) to estimate the relative weight fractions of each crystalline component. XAS measurements were performed at the BL1D beamline of the PLS-II (PAL). The storage ring was operated at 3.0 GeV in a top-up mode. Energy selection was achieved using a Si(111) monochromator. The data acquisition utilized a step-scan mode. Local atomic environment was analyzed using X-ray absorption fine structure (XAFS) spectroscopy (R-XAS, Rigaku, Japan), and data were processed using Athena software.

Copper concentrations were quantified by inductively coupled plasma optical emission spectroscopy (ICP-OES) using the Thermo Scientific iCAP Pro instrument equipped with the ASX-560 autosampler (Cetac Technologies). Calibration was performed using commercially available Cu elemental standards (Sigma Aldrich), from which the standard calibration curve was constructed.

Electrochemical Surface Area (ECSA) Measurement

The electrochemical surface area (ECSA) of Cu-based catalysts was calculated by comparing the double-layer capacitance (C_{dl}). Cyclic voltammetry (CV) measurements were conducted at scan rates of 20, 40, 60, 80, and 100 mV s^{-1} within the non-Faradaic potential window of −0.6 to −0.5 V vs. Hg/HgO in 1 M KOH. The C_{dl} was determined by plotting the average charging current density ($\Delta j/2$), extracted at the midpoint of the non-Faradaic potential window, against the scan rate. The slope of the resulting linear fit corresponds to C_{dl}. The roughness factor (R_f) was determined by comparing the C_{dl} of the Cu electrodes to that of bare metallic Cu foam.

$$R_f = \frac{\text{Double layer capacitance}}{\text{Double layer capacitance of Cu foam}}$$

The ECSA of each electrode was normalized using the C_{dl} of metallic Cu foam (3.4 mF cm^{-2}), which is defined as 1 cm^2. All other C_{dl} values were divided by this reference to calculate relative ECSA.

Electrochemical Measurements for Formaldehyde Oxidation in an H-cell

Electrochemical formaldehyde oxidation was performed in an H-type cell (PINE research) equipped with a three-electrode configuration. The anode and cathode chambers were separated by an anion exchange membrane (AEM, SelemionAMVN). A Cu/Cu_2O electrode was used as the anode, and Ni foam served as the cathode. A saturated calomel electrode (SCE, BASi Alkaline Reference Electrode) was used as the reference electrode to monitor the electrode potential. The catholyte consisted of 35 mL of 1 M KOH, while the anolyte composition was varied with different concentrations of KOH (50–2000mM, ≥85%, ACS reagent, Sigma-Aldrich) and formaldehyde (HCHO, 50–1000mM, 37%, Certified ACS, Fisher Chemical). Converting SCE to reversible hydrogen electrode (RHE) is utilized as following equation: $E_{RHE} = E_{SCE} + 0.118 + (0.059 \times pH)$.

The pH of the electrolyte was measured using a pH meter (Orion Versa Star Pro, Thermo Scientific; **Table S4**). Linear sweep voltammetry (LSV) was performed at a scan rate of 5 mV s^{-1} within the potential window relevant to formaldehyde oxidation. For electrolyte composition-dependent experiments, each LSV measurement was repeated at least three times to ensure reproducibility and iR compensation was applied to account for ohmic losses. Chronoamperometry (CA) or chronopotentiometry (CP) was conducted to quantify hydrogen evolution, with high-purity N_2 gas (99.999%) purged into the headspace of the H-type cell as a carrier gas. The resulting H_2 and N_2 gases were analyzed using gas chromatography and formate was measured using high-performance liquid chromatography. Details of the products analysis are provided in the following section.

Electrochemical Measurements for Bicarbonate and Formaldehyde Electrolysis in Membrane Electrode Assembly (MEA)

Full-cell electrolysis for bicarbonate electrolysis (BCE) and formaldehyde oxidation reaction (FOR) was conducted using a membrane electrode assembly (MEA) reactor (Scribner). The MEA system consists of graphite plates with interdigitated flow fields and a Teflon gasket. A Ni-SAC electrode with a geometric area of 1 cm^2 was used as the cathode, while a Cu/Cu_2O electrode of the same area was employed as the anode. The Cu/Cu_2O electrode was rinsed with deionized (DI) water and immediately used following the activation process. A commercial bipolar membrane (*c*-BPM, ACM-IM-002, Alfa-Chemistry) or a synthetic bipolar membrane (*s*-BPM) was placed between the two electrodes. The catholyte, 100mL of 3 M $KHCO_3$ (99.7%−100.5%, ACS reagent, Fisher Scientific) continuously bubbled with CO_2 at 400 sccm controlled by mass flow controller (MFC, Alicat), was circulated through the interdigitated flow plate at a rate of 30 mL min^{-1} using a Masterflex L/S peristaltic pump. Before being introduced into the gas chromatograph (GC, SRI Instruments, SRI 8610C), the gaseous products were passed through a dryer, with high-purity N_2 (99.999%, Airgas) used as the carrier gas at a rate of 100 sccm. For the FOR at the anode, 100 mL of anolyte containing 1 or 2 M HCHO and 1 or 2 M KOH was circulated at a flow rate of 30 mL min^{-1}. Produced H_2 gas is carried by N_2 at a rate of 200 sccm to the dryer and GC. Gas products from both cathode and anode were simultaneously analyzed using two GCs. The concentrations of N_2, H_2, and CO were determined using a thermal conductivity detector (TCD) and a flame

ionization detector (FID) integrated into the GCs. Calibration was performed using 0.5% standard gases for H_2 and CO, and 100% N_2 gas.

Chronopotentiometry (CP) was conducted at current densities ranging from 100 to 600 mA cm^{-2}, with each step maintained for 30 minutes using a potentiostat (Biologic SP-150e). GCs analyzed gas products after 15 minutes of electrolysis at each step. Long-term electrolysis was performed at a constant current density of 200 mA cm^{-2} under identical conditions, except that the anolyte volume was increased to 1 L. Both the catholyte and anolyte were not replaced throughout the electrolysis, unless stated otherwise. Gas products were analyzed every hour.

Formate Measurements

Formate concentrations were analyzed using high-performance liquid chromatography (HPLC, Waters Corporation) equipped with an Aminex HPX-87H column (Bio-Rad). A UV/Visible detector (UVD, wavelength: 260 nm) and a refractive index detector (RID) were used for quantifying formate. The mobile phase was 5 mM H_2SO_4 (98%, for HPLC LiChropur™, Supelco) delivered at a flow rate of 0.4 mL min^{-1}, and the column temperature was maintained at 30 °C. Prior to analysis, liquid samples were neutralized and diluted with sulfuric acid: 1 mL of sample was mixed with 2 mL of 0.5 M H_2SO_4. Calibration for formate quantification was performed using standard solutions of 1, 10, 100, and 1000ppm.

Calculations of performance metrics

The Faradaic efficiencies of H_2, CO, and formate ($HCOO^-$) were calculated using the following equation:

$$FE = \frac{z \times n \times F}{Q}$$

where z is the number of electrons involved in product formation (2 for H_2 and CO in CO_2RR and FOR and 1 for $HCOO^-$ in FOR), n is the number of moles product obtained by GC and HPLC; F is Faradaic constant (96,484 C mol^{-1}); Q is the amount of charge transferred during electrolysis.

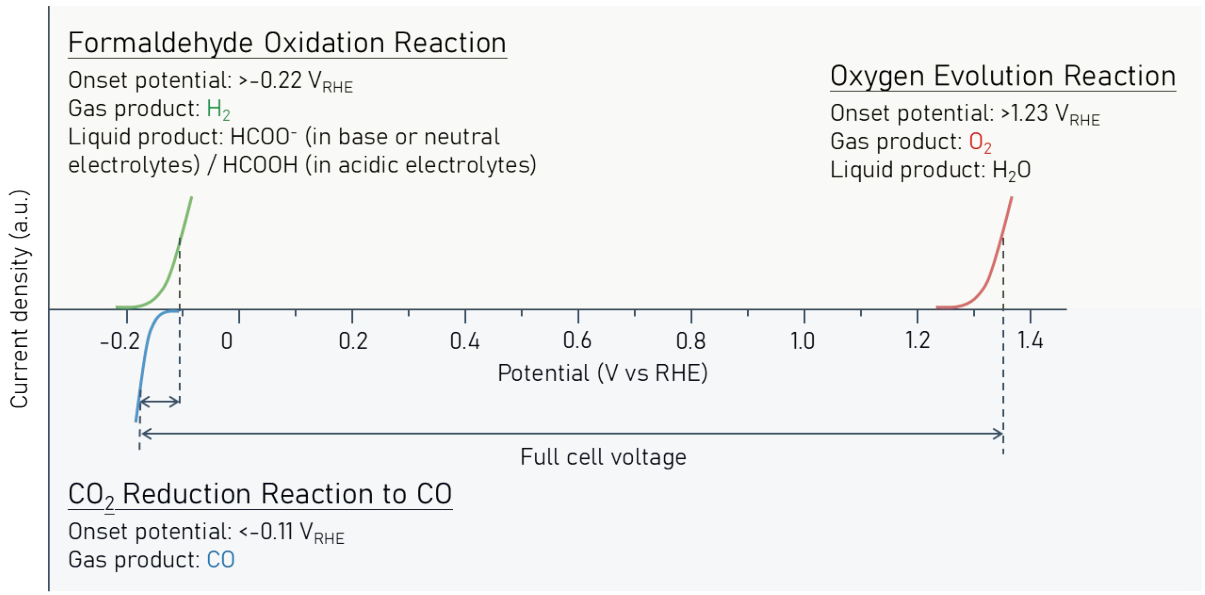

Fig. S1. Representative polarization curves showing the onset potentials for CO_2 reduction to CO, formaldehyde oxidation (as a model aldehyde), and the oxygen evolution reaction (OER).

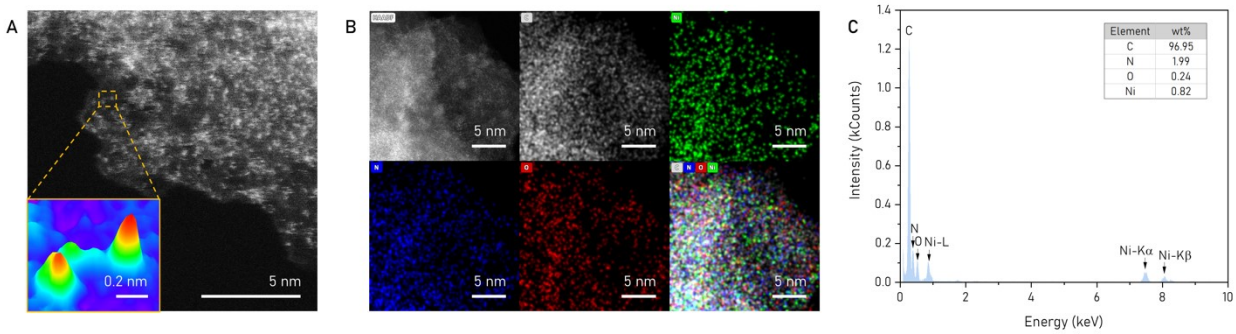

Fig. S2. Microscopic Characterization of Ni-SAC. (A) High-angle annular dark-field scanning transmission electron microscopy (HAADF-STEM) image of the Ni single-atom catalyst (Ni-SAC). The inset shows a magnified image highlighting atomically dispersed Ni atoms (indicated by red regions). (B) STEM-energy-dispersive X-ray spectroscopy (STEM-EDS) elemental mapping images of Ni-SAC, confirming the uniform distribution of C (white), Ni (green), N (blue), and O (red). The corresponding HAADF-STEM image is shown alongside. (C) STEM-EDS spectrum of Ni-SAC, indicating elemental compositions of 1.99 wt% N and 0.82 wt% Ni in the prepared Ni-SAC.

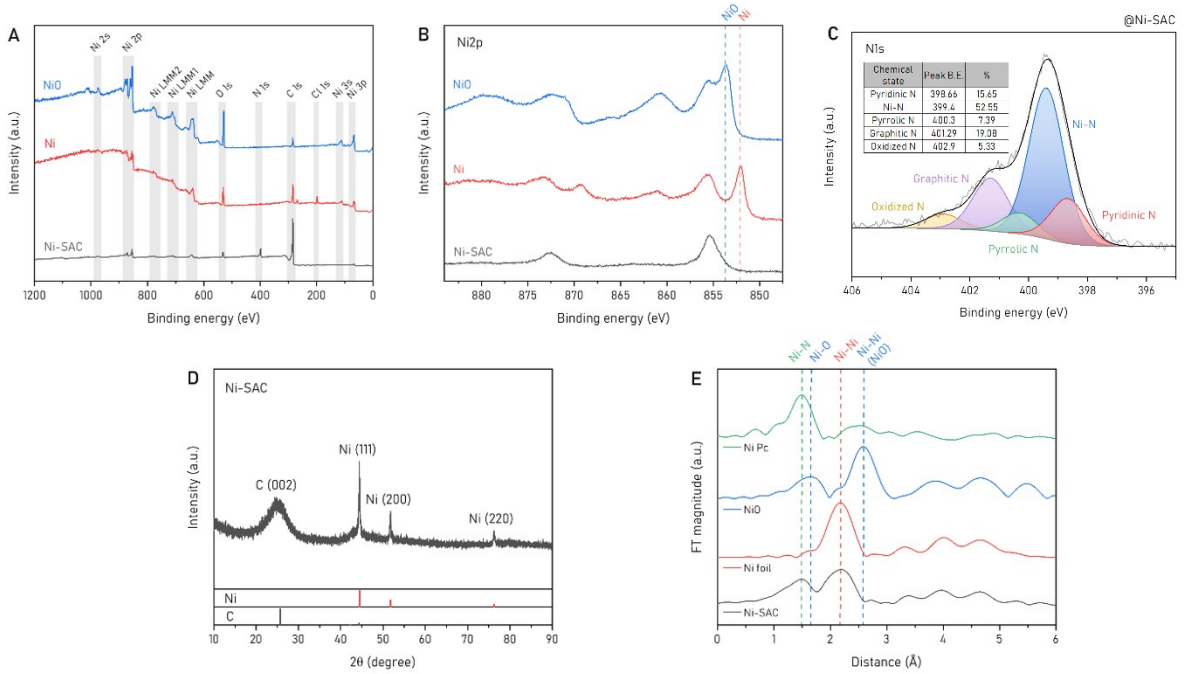

Fig. S3. Physicochemical characterization of Ni-SAC. (A) X-ray photoelectron spectroscopy (XPS) survey spectra of Ni-SAC, metallic Ni, and NiO. (B) High-resolution Ni 2p XPS spectra of Ni-SAC, Ni, and NiO. The Ni-SAC sample exhibits a unique main peak without satellite features, which are typically associated with oxidized Ni species. This suggests that the majority of surface Ni exists as atomically dispersed active sites. (C) High-resolution N 1s XPS spectrum of Ni-SAC, deconvoluted into five components corresponding to pyridinic N, pyrrolic N, graphitic N, oxidized N, and Ni–N bonding. The presence of the Ni–N peak confirms that Ni atoms are coordinated with N. (D) X-ray diffraction (XRD) pattern of Ni-SAC, with reference patterns for Ni and C. The observed diffraction peaks, together with the XPS results, indicate the presence of Ni nanoparticles embedded within the bulk, with an estimated crystallite size of 52.2 nm. (E) Fourier-transform extended X-ray absorption fine structure (FT-EXAFS) spectra of Ni-SAC, Ni foil, NiO, and Ni phthalocyanine (Ni Pc). The EXAFS profile of Ni-SAC shows prominent Ni–N coordination, along with a Ni–Ni contribution likely originating from unavoidable nanoparticle formation during high-temperature treatment.

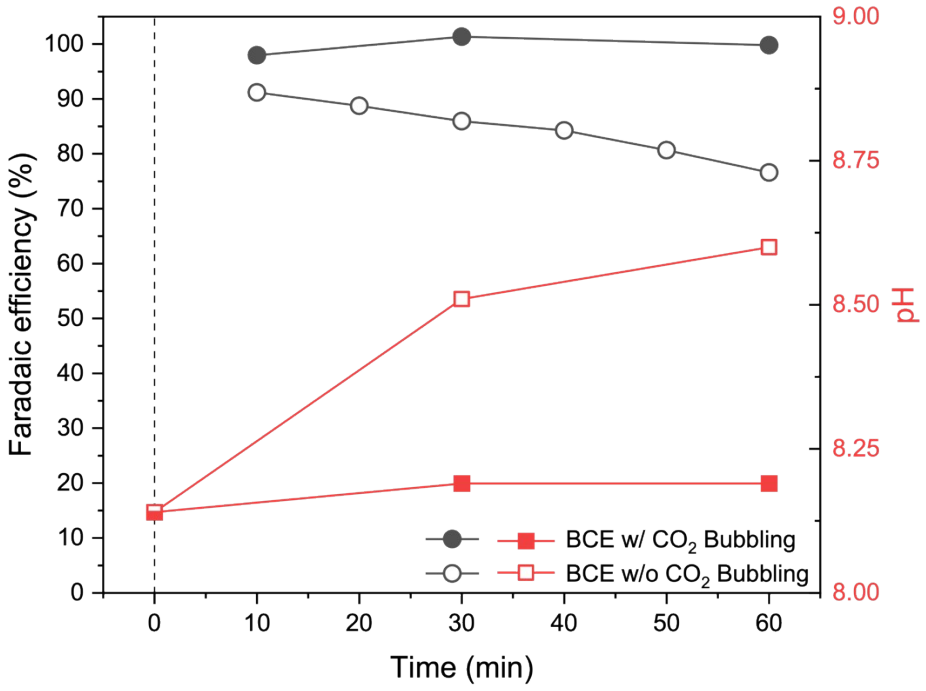

Fig. S4. Pseudo-steady-state performance of bicarbonate electrolysis. Faradaic efficiency (left axis) and pH (right axis) profiles measured at a constant current density of 200 mA cm^{-2} over time, comparing electrolysis with and without CO_2 bubbling.

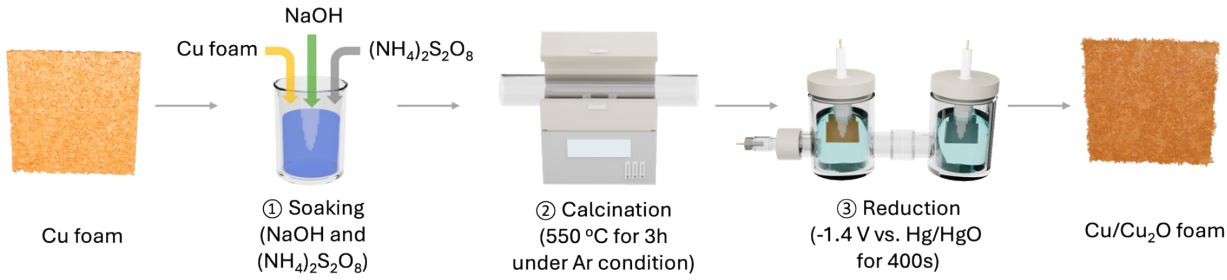

Fig. S5. Fabrication procedure of the Cu/Cu_2O electrode. Cu foam is first soaked in an alkaline solution containing NaOH and $(NH_4)_2S_2O_8$ to form $Cu(OH)_2$. The sample is then calcined at 550 °C for 3 hours under Ar atmosphere to convert $Cu(OH)_2$ into Cu_2O. Finally, partial electroreduction is performed at –1.4 V vs. Hg/HgO for 400 seconds, yielding a Cu/Cu_2O electrode.

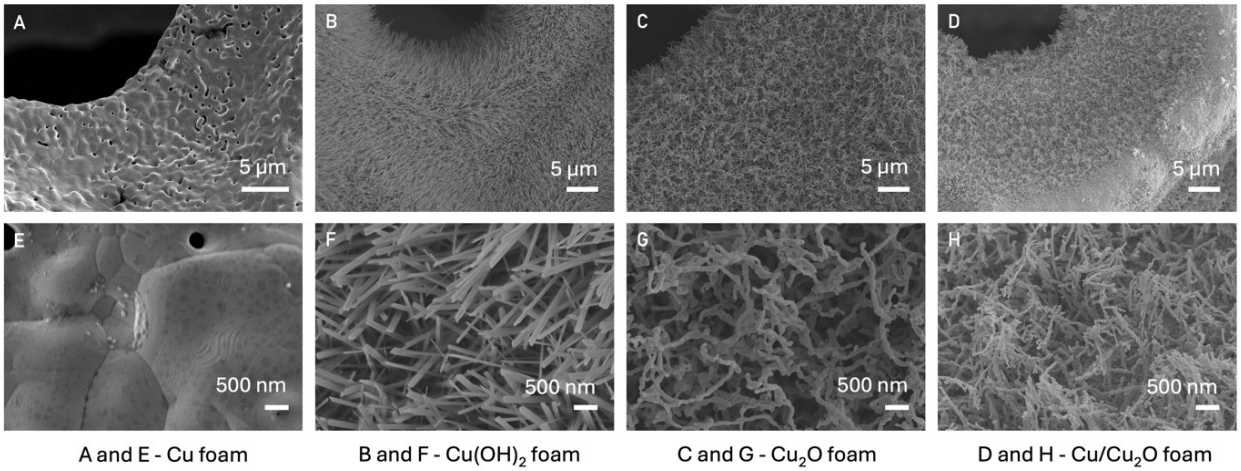

Fig. S6. Structural and morphological characterization of each step in Cu/Cu_2O synthesis. (A–D) Low-magnification SEM images of Cu foam (A), $Cu(OH)_2$ foam (B), Cu_2O foam (C), and Cu/Cu_2O foam (D). (E–H) Corresponding high-magnification SEM images of Cu foam (E), $Cu(OH)_2$ foam (F), Cu_2O foam (G), and Cu/Cu_2O foam (H), illustrating the evolution of surface morphology during the synthesis process.

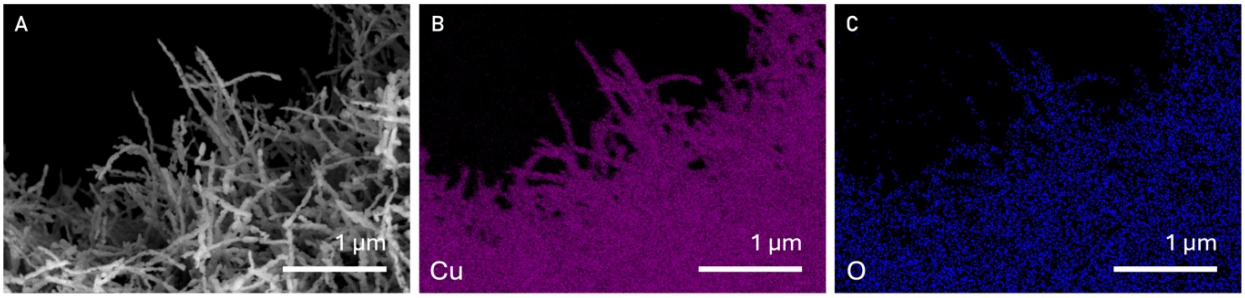

Fig. S7. SEM image and elemental mapping of the Cu/Cu_2O foam. (A) SEM image showing the nanostructured morphology of the Cu/Cu_2O foam. (B, C) EDS elemental mapping of (B) Cu and (C) O, confirming the uniform distribution of copper and oxygen throughout the structure.

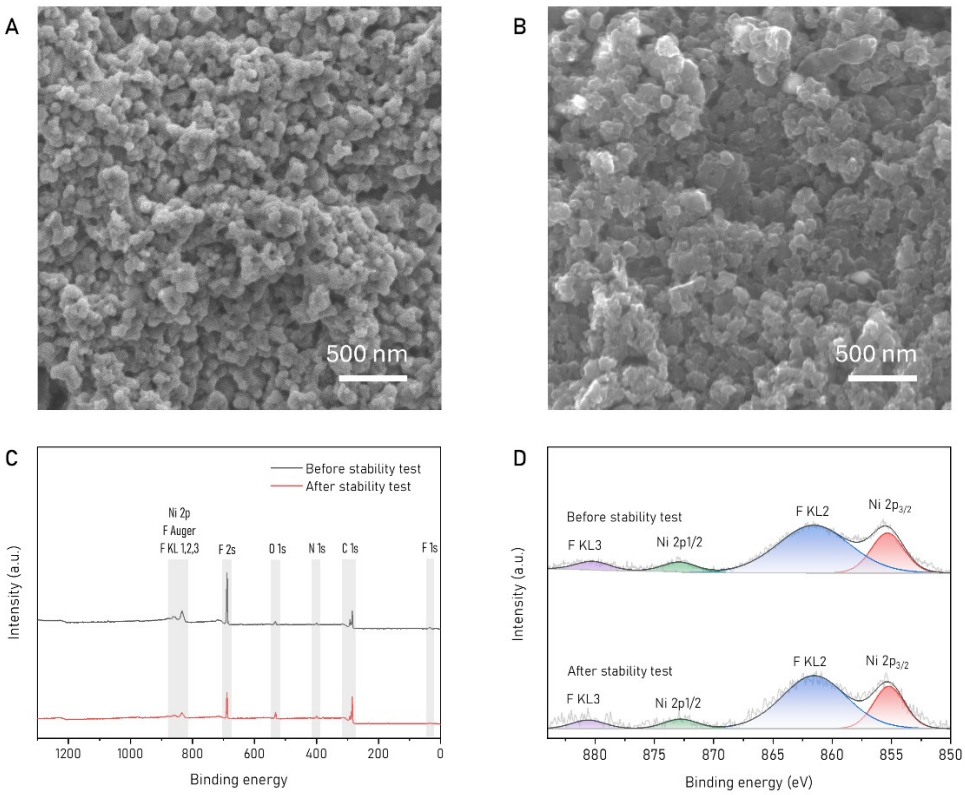

Fig. S8. Characterization of Ni-SAC electrodes before and after electrolysis. (A) SEM images of fresh Ni-SAC electrodes. (B) SEM images of Ni-SAC electrodes after electrolysis. (C) XPS survey spectra of Ni-SAC before (black) and after (red) electrolysis. (D) Ni 2p high-resolution XPS spectra of Ni-SAC before (top) and after (bottom) electrolysis.

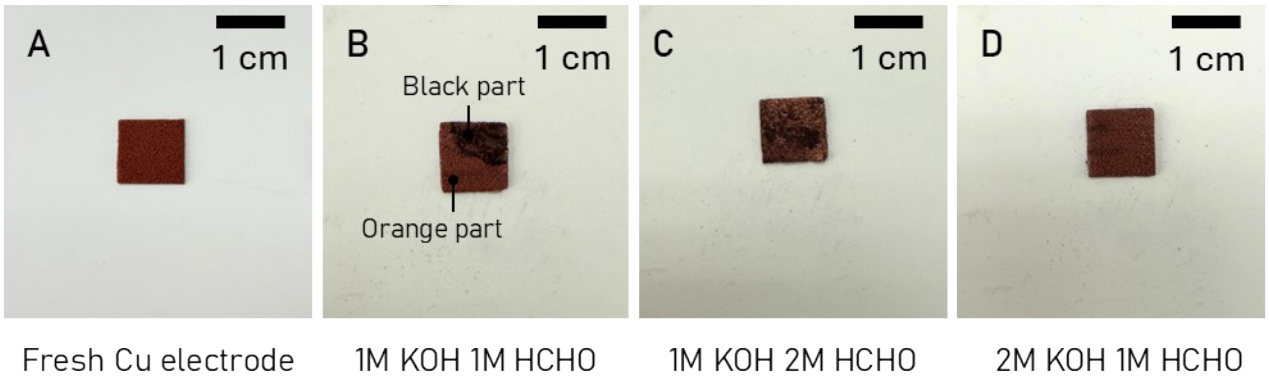

Fig. S9. Material characterization of Cu/Cu_2O electrodes after electrolysis at 600 mA cm^{-2}. Optical images of Cu/Cu_2O samples: (A) fresh, and post-electrolysis in (B) 1 M KOH with 1 M HCHO, (C) 1 M KOH with 2 M HCHO, and (D) 2 M KOH with 1 M HCHO.

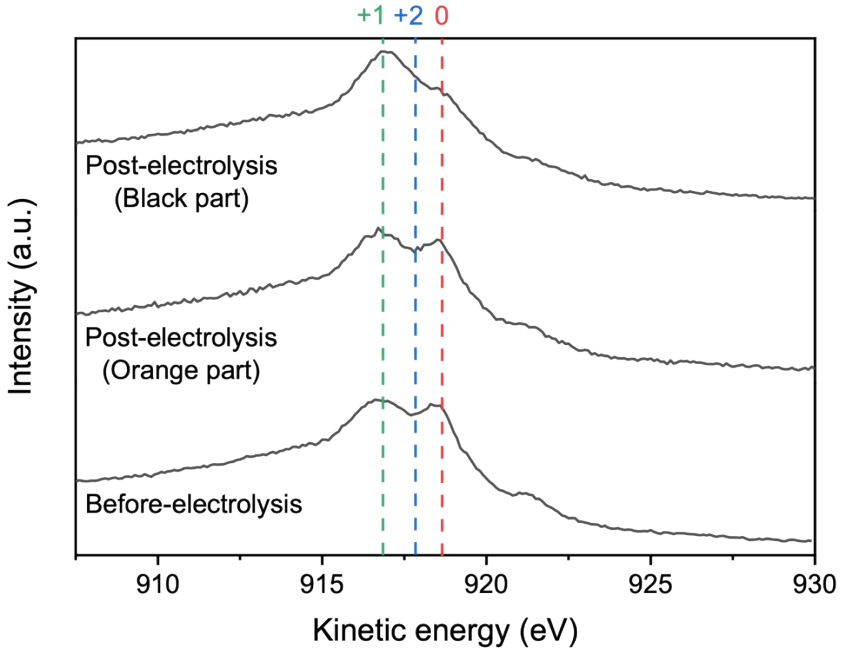

Fig. S10. Material characterization of Cu/Cu_2O electrodes after electrolysis at 600 mA cm^{-2} in 1 M KOH and 1 M HCHO electrolyte. Cu LMM Auger spectra comparing the oxidation states of the black and orange regions after electrolysis with the pristine Cu/Cu_2O electrode. Cu^0, Cu^+ and Cu^{2+} signals are indicated.

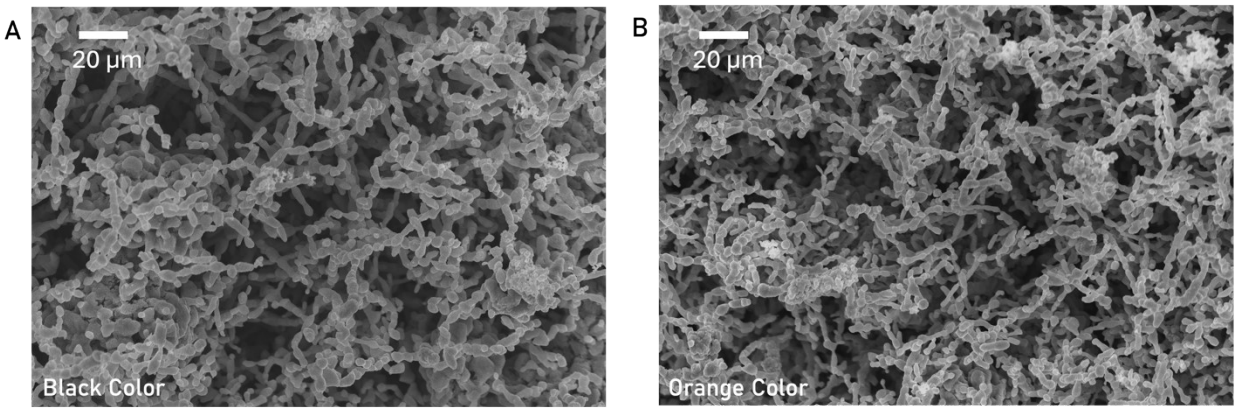

Fig. S11. Material characterization of Cu/Cu_2O electrodes after electrolysis at 600 mA cm^{-2} in 1 M KOH and 1 M HCHO electrolyte. SEM images of the post-electrolysis Cu/Cu_2O electrode corresponding to the (A) black-colored and (B) orange-colored regions.

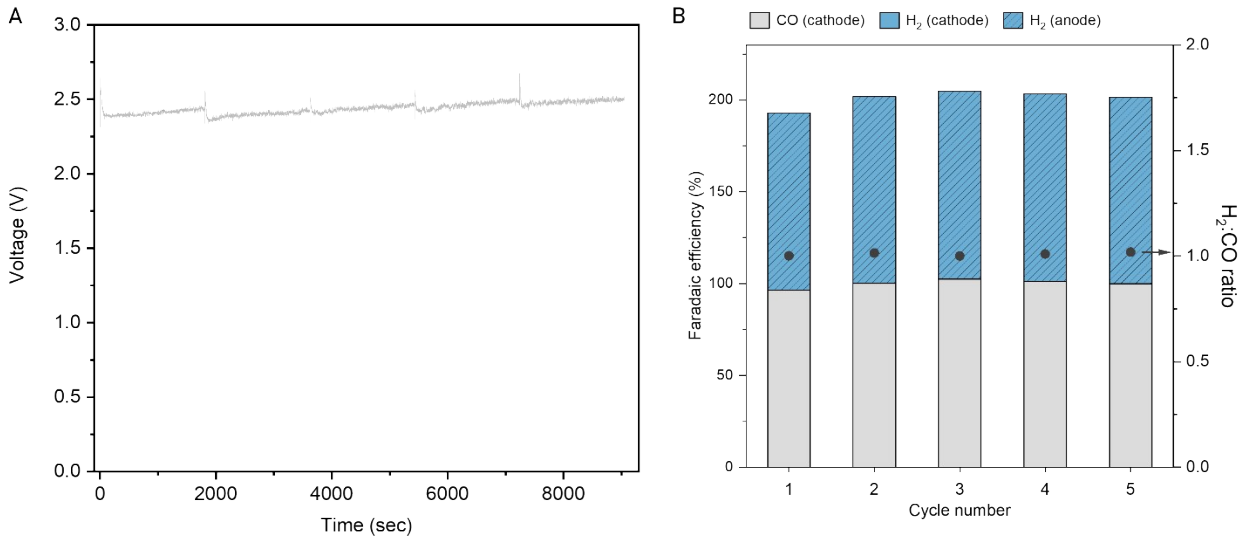

Fig. S12. Stability test of the BCE-FOR system at 200 mA cm^{-2} in 1 M KOH and 1 M HCHO electrolyte. (A) Cell voltage profile over 150 minutes of continuous operation. Formaldehyde solution was refreshed every 30 minutes. (B) Faradaic efficiencies and H_2:CO ratio for each cycle, showing contributions from CO and H_2 at the cathode and H_2 at the anode.

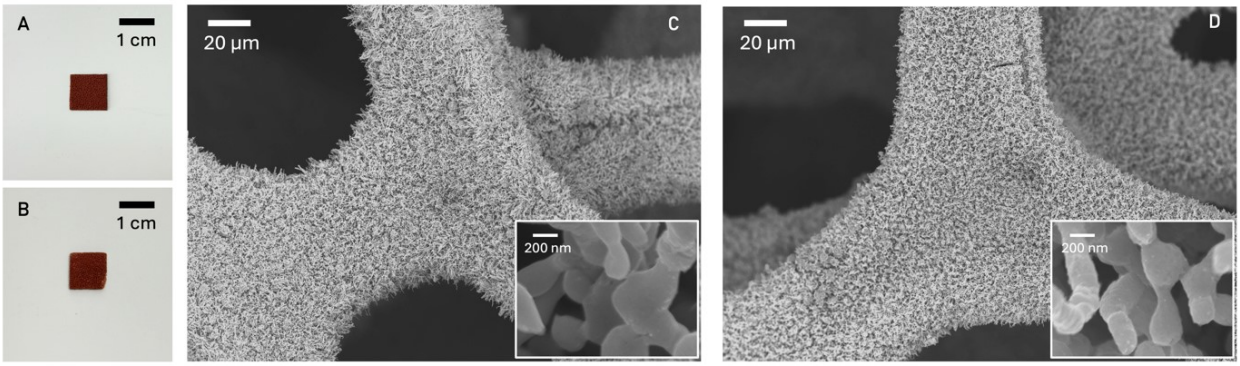

Fig. S13. Morphological characterization of Cu/Cu_2O before and after electrolysis at 200 mA cm^{-2} in 1 M KOH and 1 M HCHO electrolyte. (A, B) Optical images of the Cu/Cu_2O electrode (A) before and (B) after electrolysis. (C, D) SEM images of the Cu/Cu_2O foam (C) before and (D) after electrolysis. Insets show high-magnification views highlighting the surface features of the nanostructured Cu/Cu_2O.

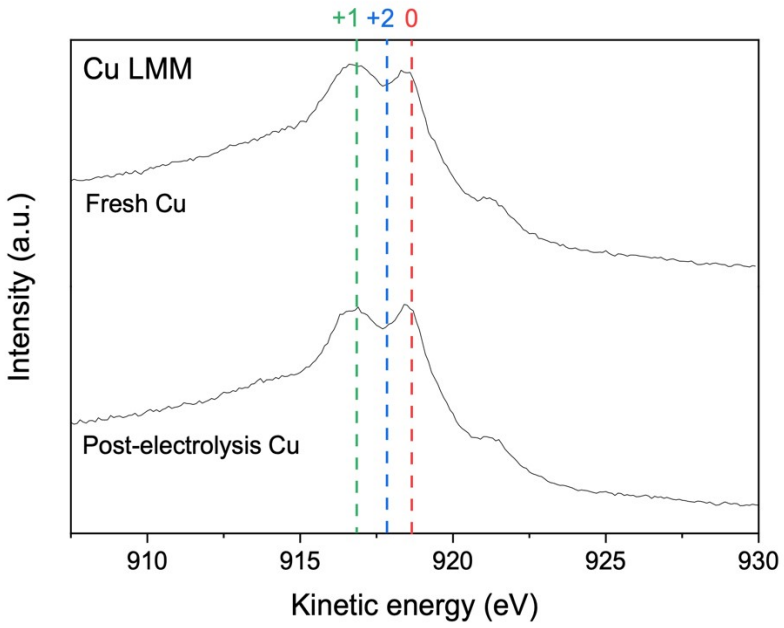

Fig. S14. Cu LMM Auger spectra of Cu/Cu_2O before and after electrolysis at 200 mA cm^{-2} in 1 M KOH and 1 M HCHO electrolyte. The presence of both Cu^0 and Cu^+ is observed in the fresh and post-electrolysis samples.

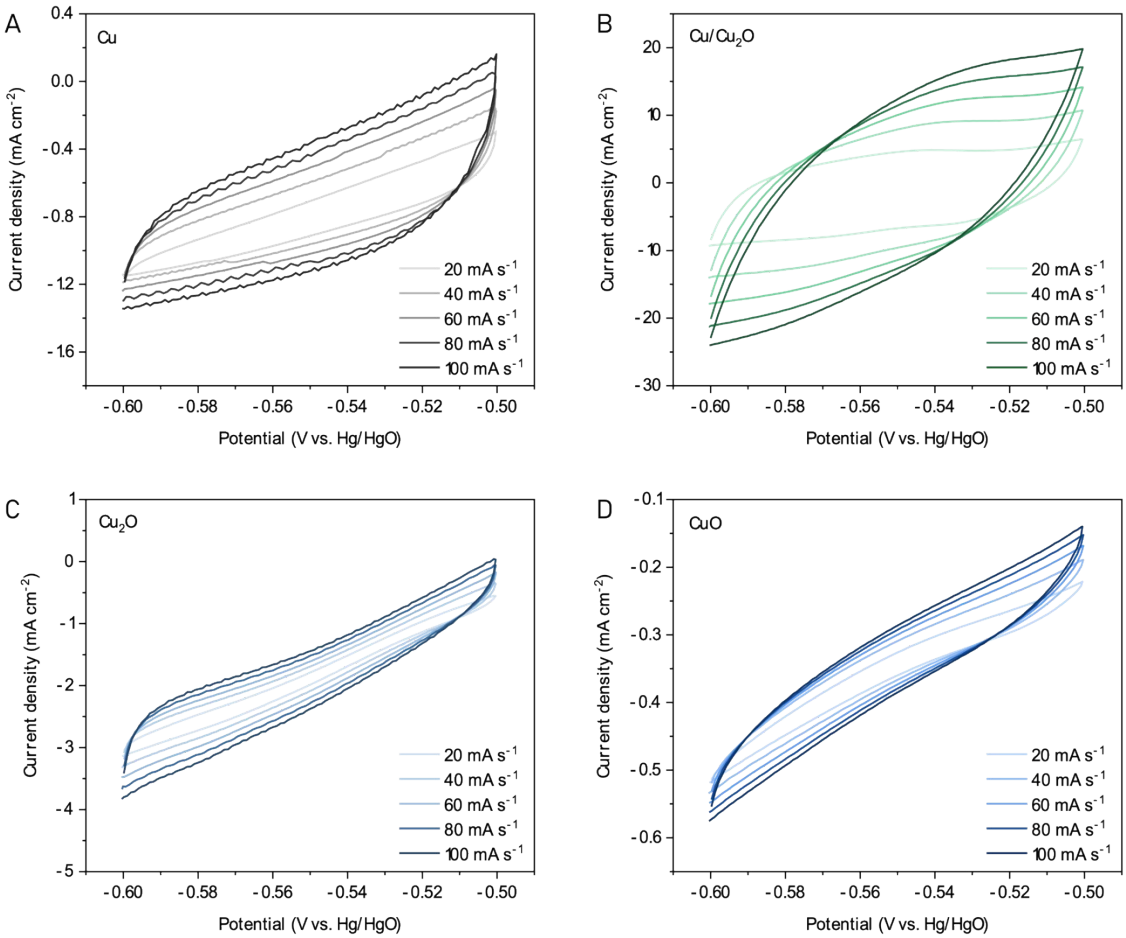

Fig. S15. Cyclic voltammetry (CV) of (A) Cu, (B) Cu/Cu_2O, (C) Cu_2O, and (D) CuO. Measurements taken ±50 mV from −0.55 V (vs. Hg/HgO) at scan rates of 20, 40, 60, 80, and 100 mV sec^{-1}.

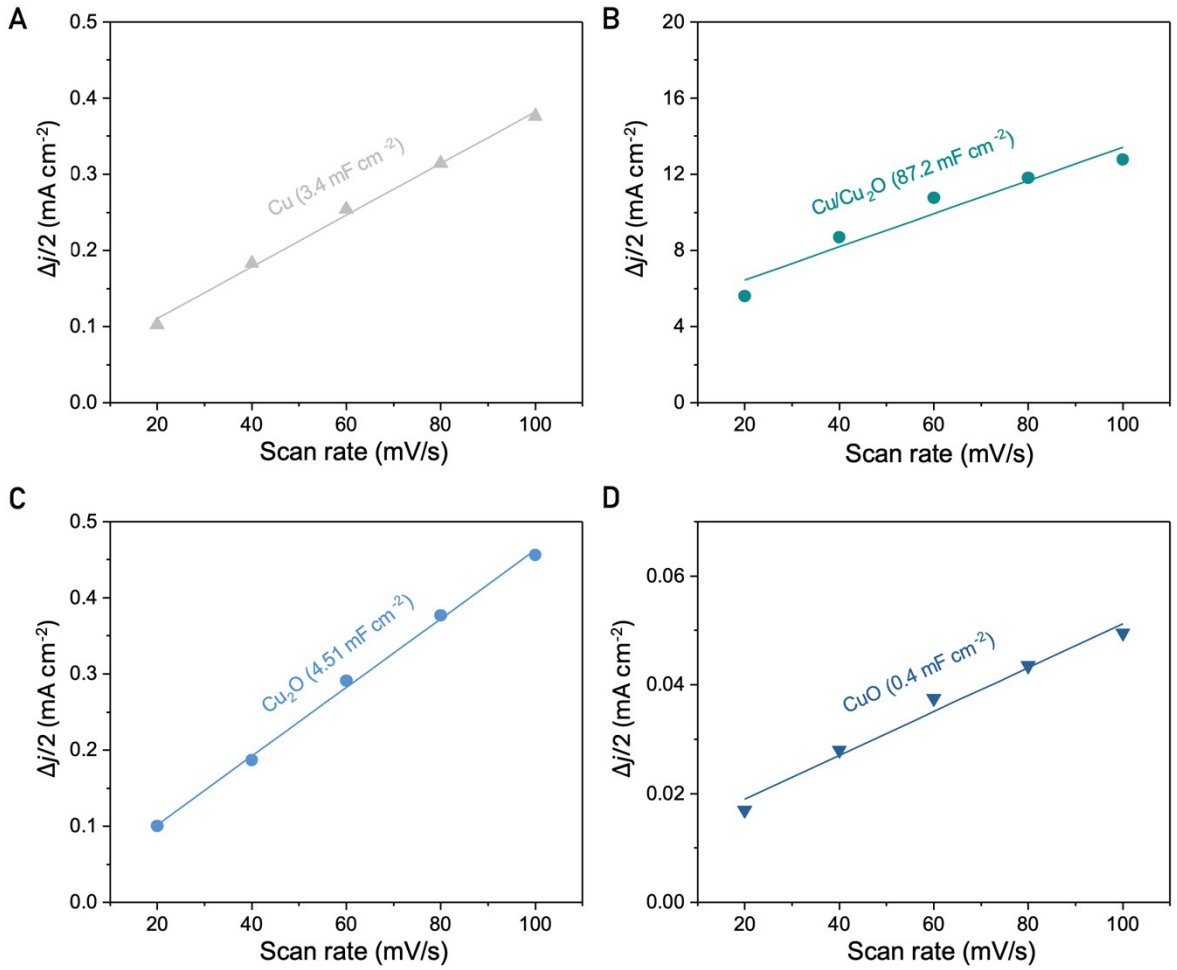

Fig. S16. Electrochemical double-layer capacitance (C_{dl}) of (A) metallic Cu foam, (B) Cu/Cu_2O, (C) Cu_2O, and (D) CuO.

Table S1. Calculation of double layer capacitance, roughness factor and ECSA

	Sample	Double-layer Capacitance (mF cm^{-2})	Roughness Factor	ECSA (cm^2)
1	Cu	3.4	1	1*
2	Cu/Cu_2O	87.2	25.7	25.7
3	Cu_2O	4.51	1.33	1.33
4	CuO	0.4	0.12	0.12

*The ECSA of Cu was set to 1 cm^2 as a reference.

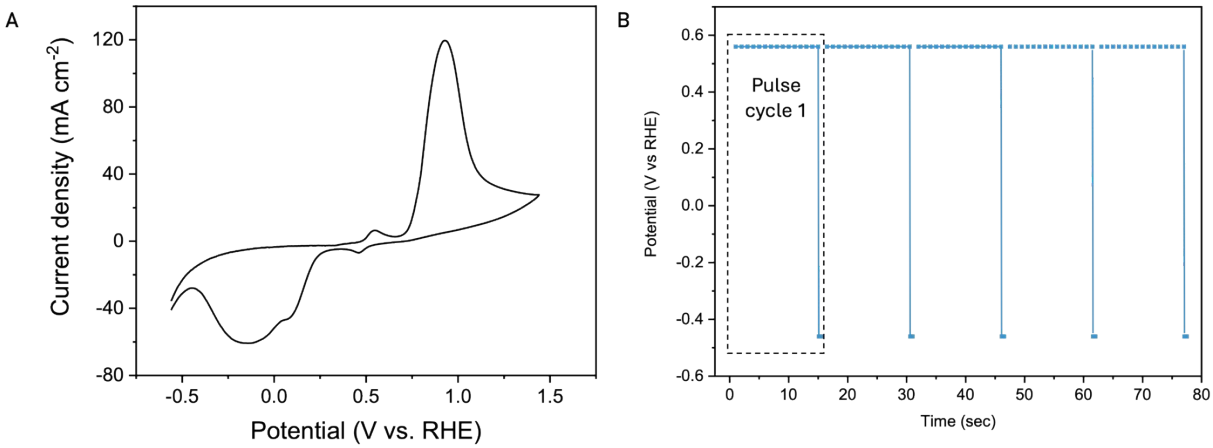

Fig. S17. Electrochemical pulsed treatment for Cu/Cu_2O synthesis. (A) Cyclic voltammetry (CV) of metallic Cu foam in 1 M KOH with scan rate of 5mV sec^{-1}. (B) Voltage-time profile showing cyclic pulsing between oxidative (+0.56 V vs. RHE) and reductive (–0.46 V vs. RHE) potentials applied to a metallic Cu foam. The repetitive redox cycling facilitates the formation of Cu/Cu_2O through controlled surface oxidation and reduction. The first pulse cycle is indicated by the dashed box.

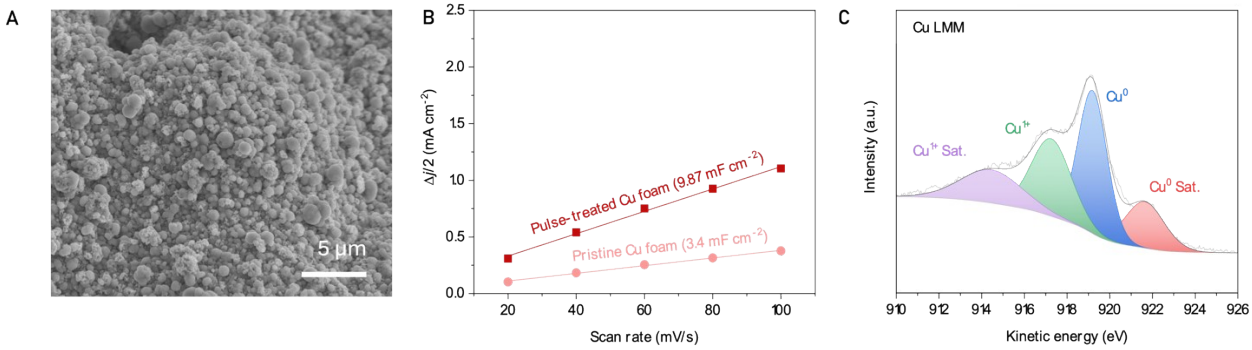

Fig. S18. Material characterization of electrochemically pulse-treated Cu electrodes. (A) SEM image of the pulse-treated Cu foam electrode. (B) Double-layer capacitance (C_{dl}) measurements of pristine and pulse-treated Cu foams. (C) Cu LMM Auger spectra of the pulse-treated Cu electrode, deconvoluted into contributions from Cu^0, Cu^+, and Cu^{2+} species.

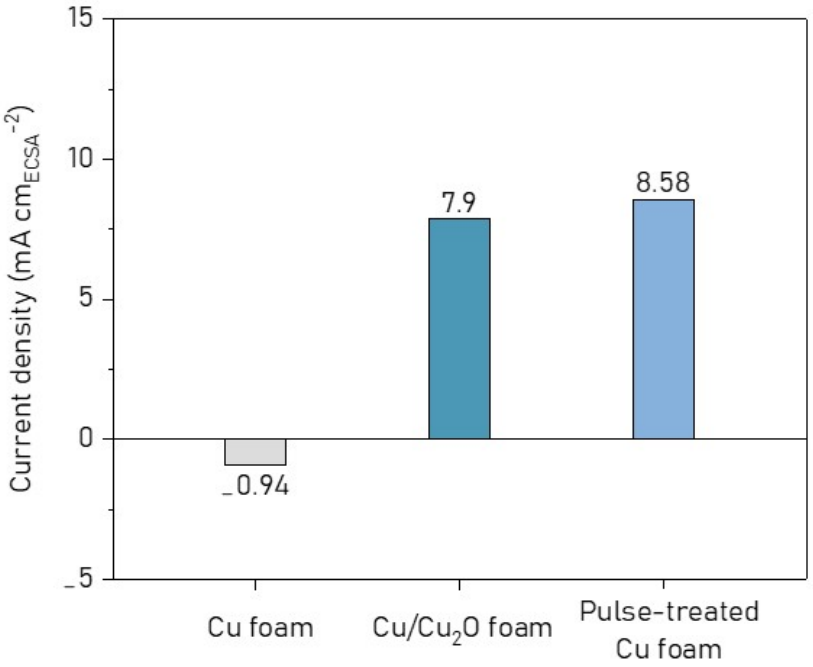

Fig. S19. Intrinsic activity for FOR. ECSA-normalized current density of Cu foam, Cu/Cu_2O foam, and pulse-treated Cu foam electrodes.

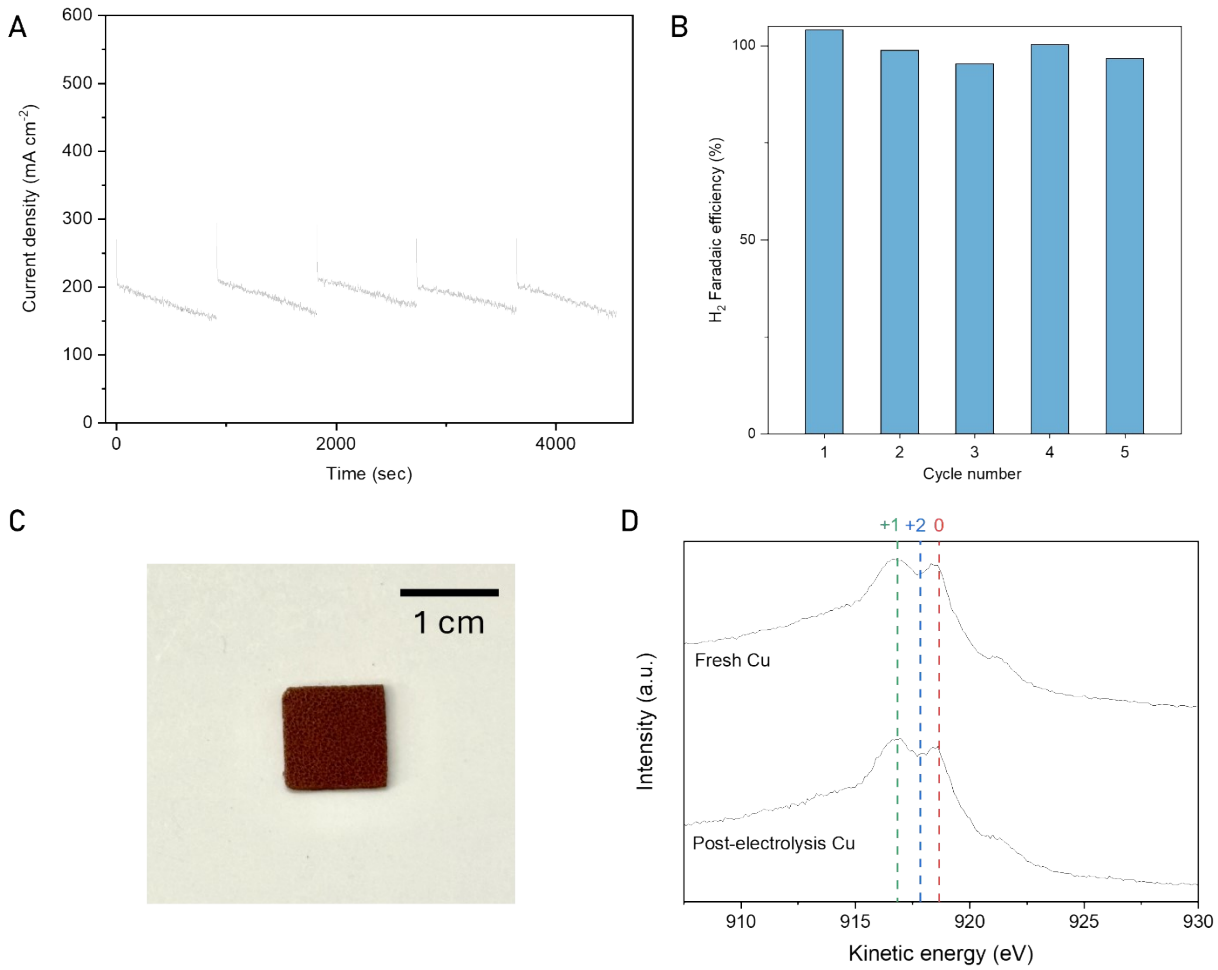

Fig. S20. Performance evaluation of the Cu/Cu_2O electrode. (A) Chronoamperometry (CA) profile of Cu/Cu_2O operated at 0.39 V vs. RHE in an H-type cell with 1 M KOH and 200 mM HCHO. The electrolyte was refreshed every 30 minutes. (B) H_2 Faradaic efficiency for each electrolysis cycle. (C) Image of the Cu/Cu_2O electrode after 5 cycles of electrolysis. (D) Cu LMM Auger spectra of the fresh and post-electrolysis Cu/Cu_2O electrodes.

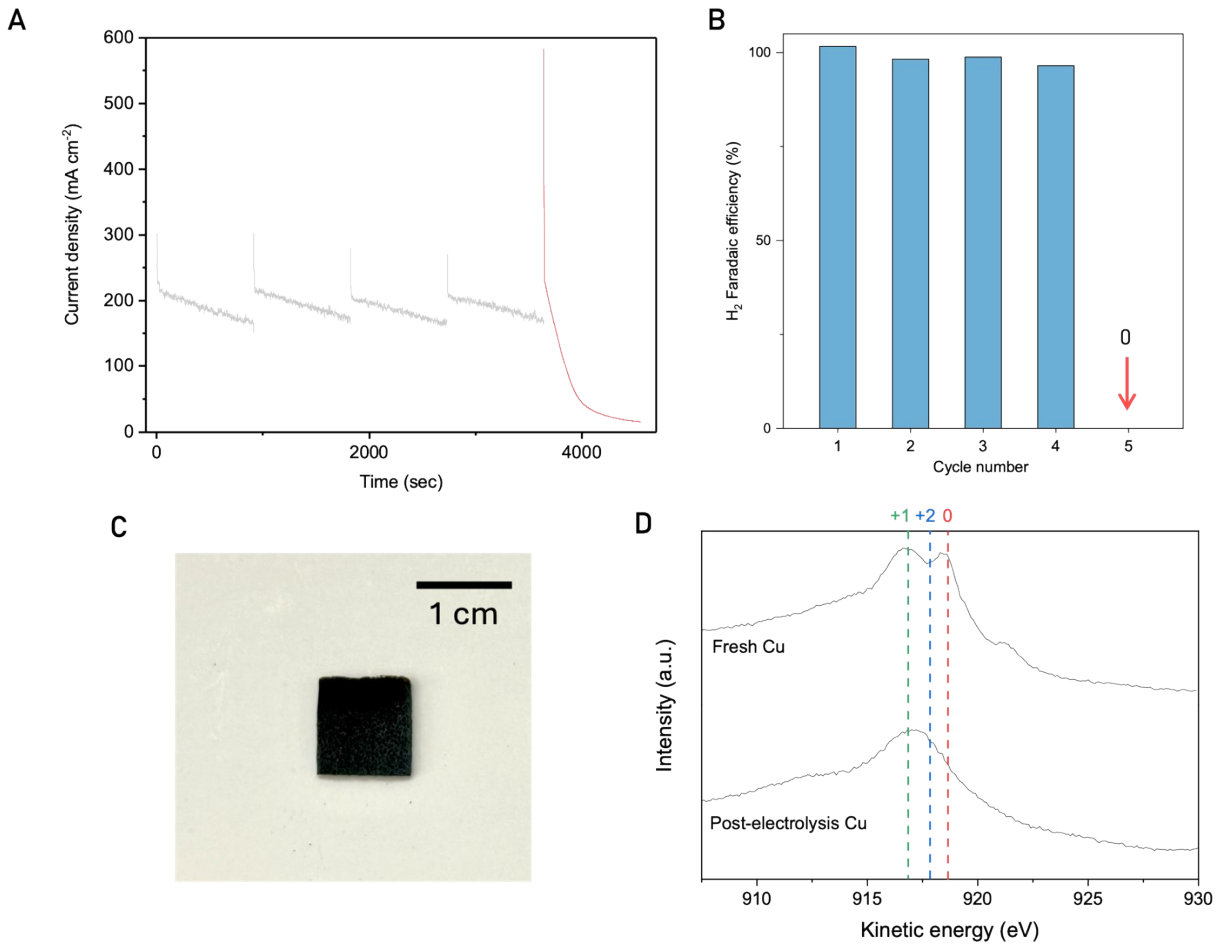

Fig. S21. Performance degradation of the Cu/Cu_2O electrode under high-potential electrolysis. (A) CA profile of Cu/Cu_2O operated at 0.39 V vs. RHE in an H-type cell using 1 M KOH and 200 mM HCHO for four cycles. The electrolyte was refreshed every 30 minutes. In the fifth cycle, a higher potential of 0.94 V vs. RHE was applied. (B) H_2 Faradaic efficiencies over five cycles. A complete loss of H_2 generation (0% FE) is observed in the fifth cycle under 0.94 V. (C) Optical image of the electrode after the fifth cycle. (D) Cu LMM Auger spectra of the fresh and post-electrolysis electrodes.

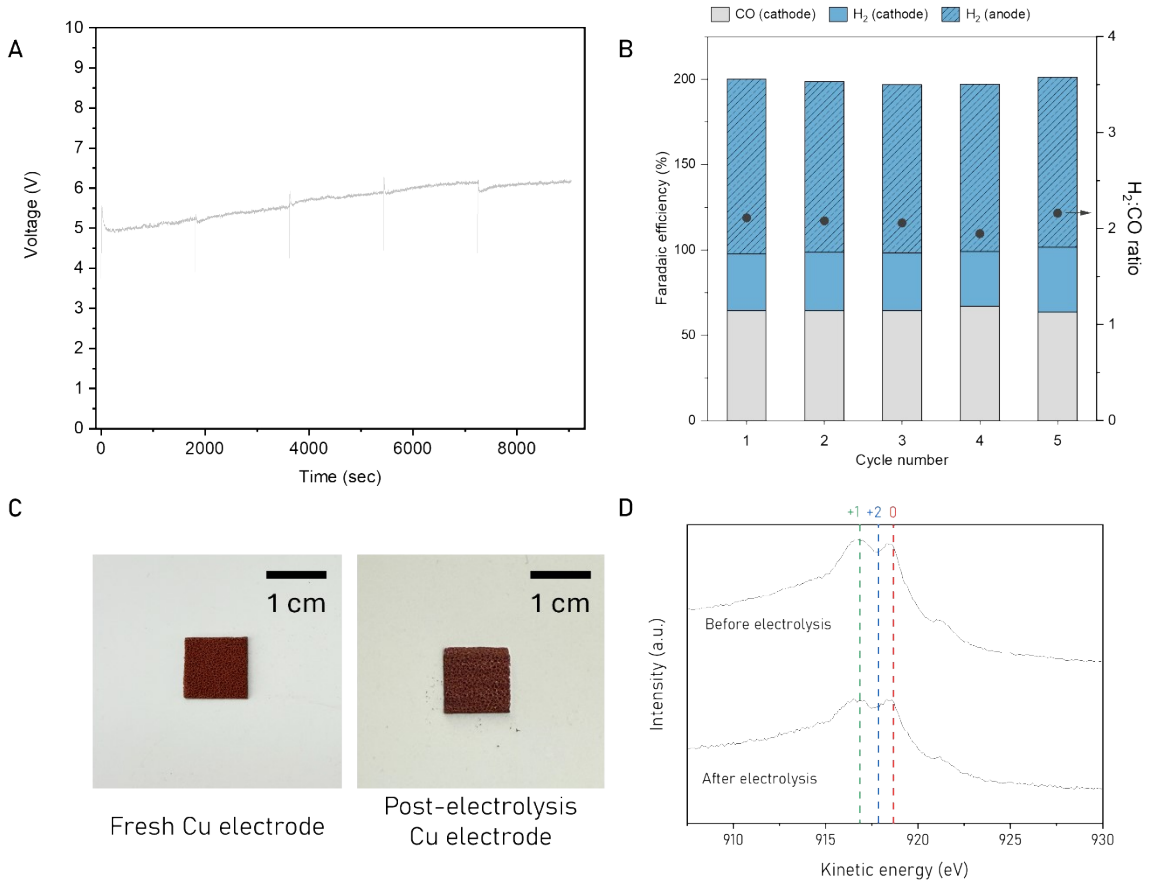

Fig. S22. Stability test of the BCE-FOR system at 500 mA cm^{-2} in 2 M KOH and 1 M HCHO electrolyte. (A) Cell voltage profile over 150 minutes of continuous operation. Formaldehyde solution was refreshed every 30 minutes. (B) Faradaic efficiencies and H_2:CO ratio for each cycle, showing contributions from CO and H_2 at the cathode and H_2 at the anode. (C) Optical images of the fresh and post-electrolysis Cu/Cu_2O electrodes. (D) Cu LMM Auger spectra of the fresh and post-electrolysis Cu/Cu_2O electrodes.

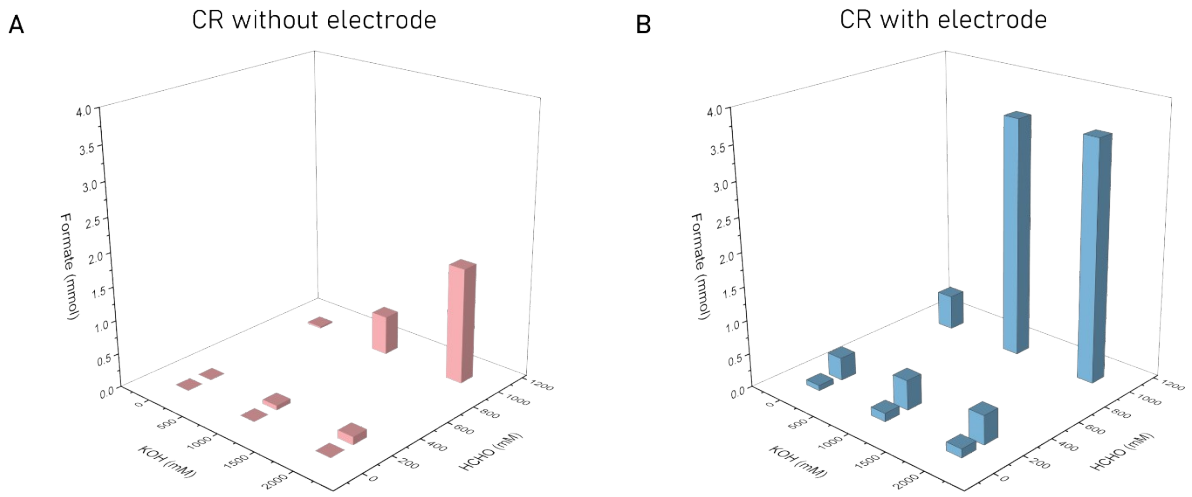

Fig. S23. Cannizzaro reaction (CR)-driven formate production under varying KOH and HCHO concentrations. (A) Formate concentrations obtained from the CR in the absence of electrodes, as a function of KOH and HCHO concentrations. (B) Formate concentrations obtained from the CR in the presence of Cu/Cu_2O electrode under open circuit potential and identical chemical conditions.

Table S2. Ratio comparison of Cannizaro reaction (CR) to formaldehyde oxidation (FOR)

- CR:FOR ratio at 0 V_{RHE}

	50	**1000**	**2000**	**KOH (mM)**
50	0.95	0.47	0.48	
200	4.00	0.95	0.88	
1000	32.43	7.77	3.92	
HCHO (mM)				

- CR:FOR ratio at 0.18 V_{RHE}

	50	**1000**	**2000**	**KOH (mM)**
50	0.31	0.22	0.26	
200	1.10	0.19	0.15	
1000	2.12	1.03	0.29	
HCHO (mM)				

Notes: The formate generated via FOR, denoted as $formate_{FOR}$, is calculated based on the total charge passed through the electrode during a 15 minute chronoamperometry (CA) test at 0 V or 0.18 V vs RHE. We assume that under the same HCHO and KOH concentrations, the contribution from homogeneous CR remains constant ($formate_{CR\_solution}$, Fig. S23A). The heterogeneous CR contribution (i.e., CR occurring on the electrode surface; $formate_{CR\_surface}$) is calculated as:
$formate_{CR\_surface}$ = total formate after CA test − $formate_{FOR}$ − $formate_{CR\_solution}$

The ratio reported here is calculated as:
CR:FOR ratio = $formate_{CR\_surface}$ / $formate_{FOR}$

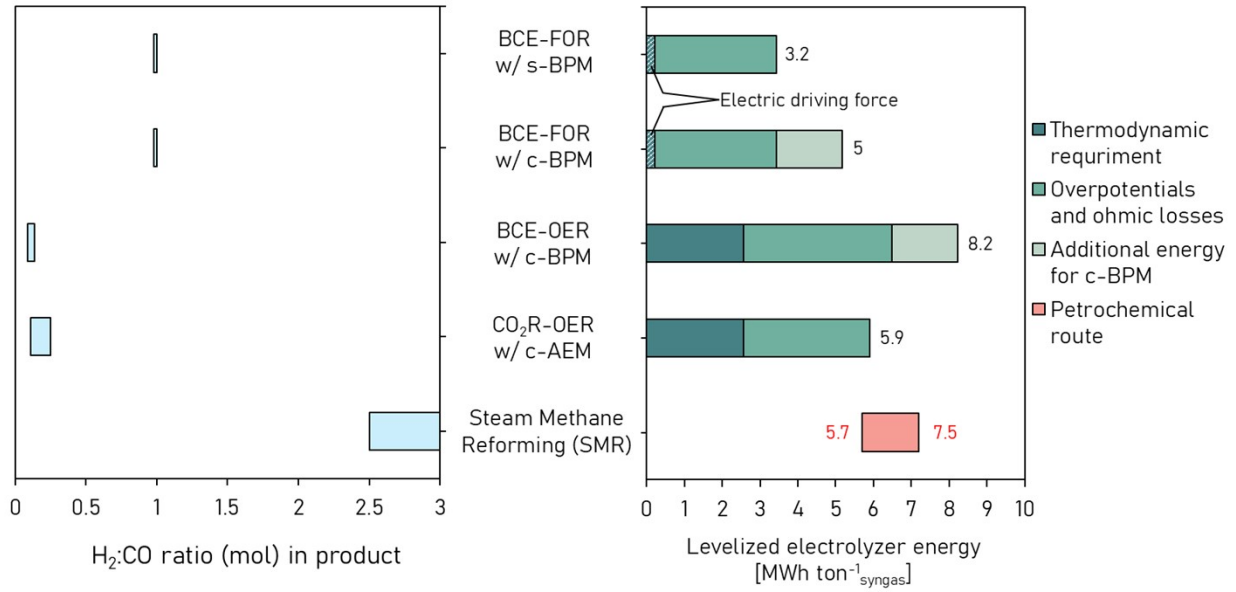

Fig. S24. Syngas ratio and electrolyzer energy intensity in electrochemical routes. The corresponding H_2:CO molar ratios in the syngas product, derived from simple Faradaic calculations, are shown in the left panel. The levelized energy required for the electrolyzer alone, normalized per ton of syngas produced, is shown in the right panel. As a reference, the full-process energy demand of the steam methane reforming (SMR-based) route ranges from 5.7−7.5 MWh/ton syngas.[3] The AEM configuration assumes 90% Faradaic efficiency toward CO at 200 mA cm^{-2}. The hatched segment in the BCE-FOR cases denotes the thermodynamic "electric driving force" arising from the positive E_{cell} of FOR-coupled operation (galvanic character). In this levelized-energy metric, values represent external electricity input required and are therefore plotted as non-negative; the hatched segment should be interpreted as an offset to purchased electricity (chemical energy supplied by the anodic organic reactant), not as net electricity generation.

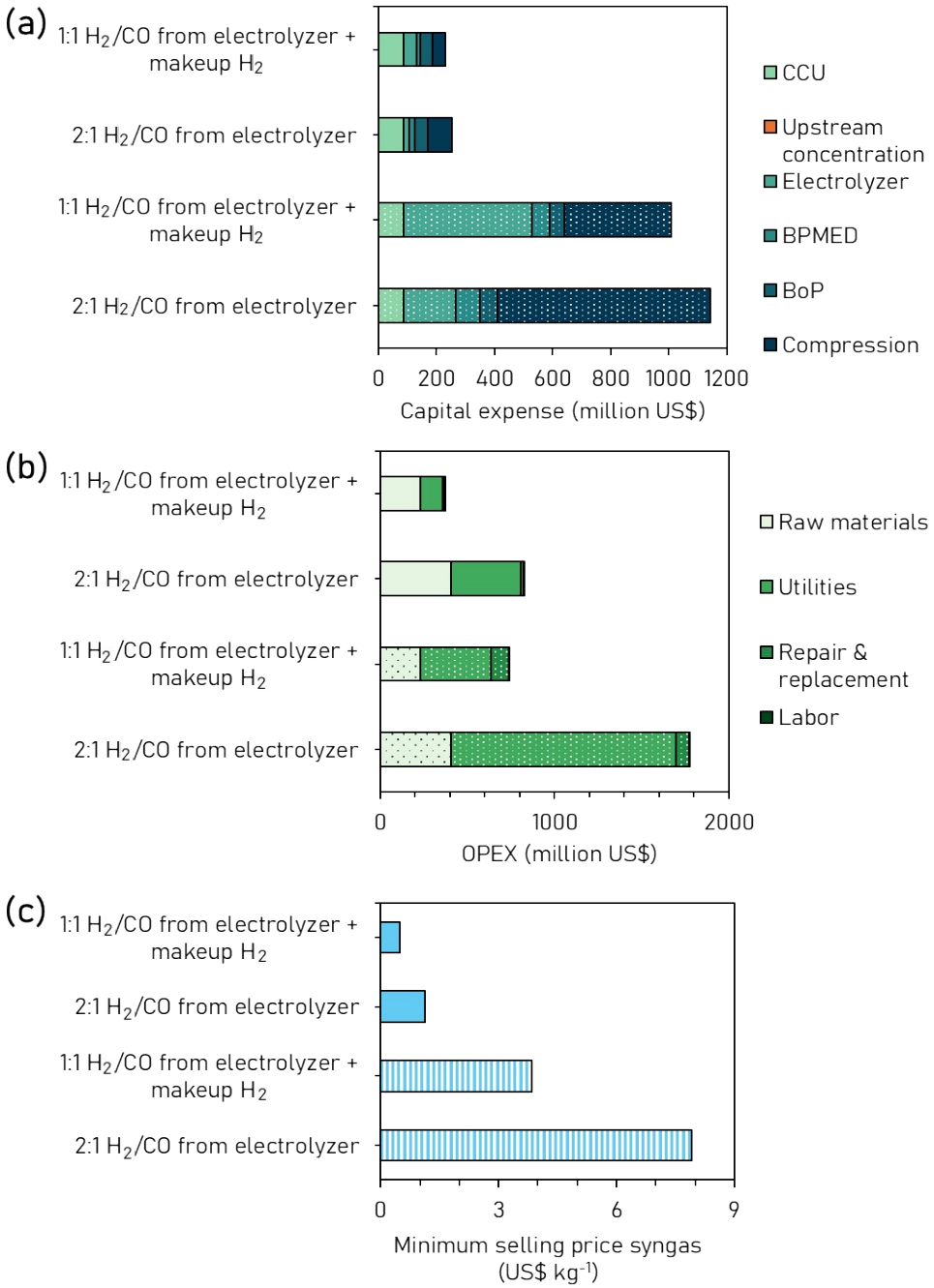

Fig. S25. Scenario comparison of the techno-economic results for the integrated process. Panel **(a)** shows the fixed-capital investment (FCIL) breakdown by major process unit, panel **(b)** shows the annual operating-cost breakdown (electricity/consumables and other OPEX terms as grouped in the legend), and panel **(c)** shows the corresponding energy (electricity) intensity contribution on the stated product basis. In each panel, the top two bars correspond to the optimistic case (solid fill) and the bottom two bars correspond to the pessimistic case (patterned fill: dotted/hatched); colors indicate the individual contributors listed in the legend, and the total bar length is the summed value for that case. The basis assumed is 200,000 TPA CO or (228570 TPA syngas with 2:1 H_2/CO ratio).

Table S3. Parameters for process designs and sensitivity analysis for production of 200,000 TPA CO or (228570 TPA syngas with 2:1 H_2/CO ratio) via the BCE-FOR case. SOA refers to current State-of-the-art conditions.

Parameter	SOA	Optimistic	Units
Carbon Capture Unit			
Capture efficiency	95	90	%
CCU CAPEX[1]	0	0	% Change[1]
Upstream GO membrane concentrator unit			
Threshold CO_3^{2-} concentration	3	1	M
Membrane permeance	2.1	2.1	$Lm^{-2}bar^{-1}h^{-1}$
CO_3^{2-} rejection	0.7	0.7	%
Membrane cost	200	175	$\$/m^2$
Membrane Lifetime	3	5	years
Electrolysis Unit			
Stack cost CAPEX[2]	0	-75	% Change[2]
Single pass conversion	60	60	%
Current density	0.6	0.6	$A.cm^{-2}$
CO faradaic efficiency (cathode)	50/100	50/100	% [3a]
H_2 faradaic efficiency (Cathode)	50/0	50/0	% [3a]
Cell Voltage[3]	10.5	10.5	V
Electrode area per cell	1	3	m^2/cell
Stack lifetime	3	7	years
Stack scaling factor	1	0.85	
Cathode catalyst factor[4]	1	0.75	
BPM lifetime	1	5	years
Loss of catalyst	5	1	%
Balance of plant			
H_2 compression cost[5]	0	-25	% Change
Scale factor for BPMED	1	0.85	
Electricity cost	0.08	0.025	US$/kWh
Green H_2 cost	5	2	US$/ kg
[1] Detailed values in the sample calculation			
[2] SOA CAPEX for the [bi]carbonate electrolyzer BPM electrolyzer as assumed as 11,476 USD/m^2			
[3] Cell voltage are based on experimentally reported values in SI Table S6. [3a] The FE values are based on experimentally reported values in main text Fig. 2B, and the 2 scenarios correspond to an electrolyzer (anode + ahhcathode) H_2/CO ratio of 1 and 2 respectively corresponding to 200 and 600 mA/cm^2 total current densities			
[4] The reference cathode uses a generic Ni catalyst, and to account for the change in cost to fabricate the Ni-SAC catalyst, a multiplicative factor is introduced			
[5] H_2-rich compression cost is assumed as 3083 \$/kWh of compression power based on https://transitionaccelerator.ca/reports/technical-brief-the-techno-economics-of-hydrogen-compression/			
The detailed description for these assumptions are summarized in Supplementary Text "Techno-economic analysis methodology".			

Table S4. Benchmarking table of CO_2 electrolysis from carbon capture solutions.

Anodic reaction	Mem--brane	Anode	Anolyte	Cathode	Catholyte	*j* (mA cm^{-2})	CO FE (%)	H_2 FE (%)	Syngas ratio	Voltage (V)	Ref.
FOR	Synthetic BPM	Cu/Cu_2O foam	2M KOH + 1M HCHO	Ni-SAC	CO_2-captured 3M $KHCO_3$	100	100.2	102.6	1.02	1.4	This work
						200	98.7	100.1	1.04	1.7	
						300	87.2	114.8	1.32	2.2	
						400	73.9	131.2	1.79	2.5	
						500	58.8	144.2	2.45	3.0	
						600	43.0	157.3	3.67	3.4	
HOR	CEM (Nafion)	Pt/C	$H_{2\,(g)}$	Ag foam	3M $KHCO_3$	100	89	11^	0.12^+	1.8	4
						500	44	56^	1.27^+	2.8	
						1000	35	65^	1.86^+	8.6	
OER	CEM (Nafion 117)	Ti-based anode	50mM H_2SO_4	Ag nano-particles (NPs)	CO_2-saturated 2M KOH	100	43	55	1.28	3.3	5
						200	47	54	1.15	3.8	
						300	34	67	1.97	4.3	
OER	CEM (Nafion 117)	Pt foil	1M KOH	Ag NPs on Ag film	CO_2-captured MEA*	50	72	38	0.53	N/A	6
						100	19	92	4.84	N/A	
OER	CEM (Nafion 115)	Ir@Ti mesh	5mM H_2SO_4	CoPc@CNT ***	3M $KHCO_3$	100	95	5^	0.05^+	3.4	7
						200	96	4^	0.04^+	4.3	
						300	96.2	3.8^	0.04^+	4.8	
OER	BPM (Fumasep FBM)	Ni foam	1M KOH	Ag NPs	3M $KHCO_3$ + 20mM EDTA**	100	84	16^	0.19^+	3.6	8
						200	68	32^	0.47^+	4.3	
						400	51	49^	0.96^+	5.6	
						800	23	77^	3.35^+	N/A	
OER	BPM (Fumasep FBM)	Ni foam	1M KOH	Ni-SAC	CO_2-captured 3M $KHCO_3$	100	97	3	0.03	3.26	9
						200	94	7	0.07	3.7	
						300	77	23	0.30	4.3	
						400	63	35	0.56	4.9	
						500	53	43	0.81	5.6	

OER	BPM (Fumasep FBM)	Ni foam	1M KOH	Ag foam	3M $KHCO_3$ + 20mM EDTA	100	95	5	0.05	3.6	10
						200	81	19	0.23	N/A	
						300	72	28	0.39	N/A	
						400	58	42	0.72	N/A	
OER	BPM (Fumasep FBM)	Ni foam	1M KOH	Ag NPs on Ag film	1M K_2CO_3	100	28	58	2.07	3.2	11
						200	31	61	1.97	3.6	
						300	24	64	2.67	4.0	
OER	Custom BPM	$NiFeO_x$ loaded Ni foam	1M KOH	CoPc–COOH bond on CNT–NH_2	3M $KHCO_3$	100	68	32^	0.47+	2.75	12
						200	63	37^	0.59+	3.13	
						300	54	46^	0.85+	3.53	
	BPM (Fumasep FBM)	Ni foam				100	70	32	0.46	3.47	
						200	67	33	0.49	4.40	
						300	60	38	0.63	5.37	
OER	BPM (Fumasep FBM)	Ni foam	1M KOH	Ni-SAC	3M $KHCO_3$	100	67.2	32.8^	0.49+	N/A	13
						200	42.7	57.3^	1.34+	N/A	
OER	BPM (Fumasep FBM)	IrO_2 loaded PtTi mesh	0.5M $KHCO_3$	Ni-SAC	CO_2-captured 5M MEA	50	64.9	35.1^	0.54+	N/A	14
OER	BPM	Ni foam	CO_2-captured 3M $KHCO_3$	Ni-SAC	CO_2-captured 3M $KHCO_3$	100	44	54	1.23	3.35	15
						200	30	71	2.37	3.94	
						300	18	82	4.56	4.47	
OER	BPM (Fumasep FBM)	Ni foam	1M KOH	Coral-Ag/C	CO_2-captured 3M TREA****	20	69	34	0.49	2.79	16
						50	47	60	1.28	3.09	
						100	36	71	1.97	3.35	
						150	29	63	2.17	3.85	
						200	29	66	2.28	4.1	
OER	BPM (Fumasep FBM)	Ni foam	1M KOH	Ag NPs	CO_2-captured 1M K_2CO_3 + 0.1M Glycine	100	30	70^	2.33+	3.51	17

OER	Custom BPM	$NiFeO_x$ loaded Ni foam	1M KOH	CoPc/PDA-HP*****	1.5M K_2CO_3	100	47	53^	1.13+	2.66	18
						200	47	53^	1.13+	2.9	
						300	46	54^	1.17+	3.21	
						400	42	58^	1.38+	3.72	
						500	41	59^	1.44+	4.14	
						600	37	63^	1.70+	N/A	

*MEA: Monoethanolamine
**EDTA: Ethylenediaminetetraacetic Acid
***CoPc@CNT: Cobalt Phthalocyanine on Carbon Nanotubes
****TREA: Triethylamine
*****CoPc/PDA-HP: CoPc-coordinated Polydopamine (PDA)-coated Hierarchically-Porous (HP) Carbon Supports.

Experiment conditions: Ref.[4] 3.5 atm/R.T.; Ref.[6] Amibent/60 ^oC; Ref.[10] 4 atm/20 ^oC; Ref.[14] Ambient/40 ^oC; The others Ambient/R.T.

Data (CO FE, H_2 FE, and voltage) from other studies were extracted from published graphs using digital image analysis.

^H_2 FE is estimated as 100% minus the reported CO FE for cases where H_2 FE is not explicitly reported.

+Syngas ratio is based on the calculated H_2 FE, estimated as 100% minus the reported CO FE.

Table S5. pH comparison with varying KOH and HCHO concentrations.

	50	**100**	**500**	**1000**	**2000**	**KOH (mM)**
0	12.72	12.96	13.68	13.99	14.31	
50	12.57	12.85	13.67	13.99	14.35	
100	12.46	12.8	13.55	13.97	14.36	
200	12.38	12.66	13.57	13.9	14.33	
500	11.98	12.32	13.32	13.83	14.3	
1000	11.64	11.94	12.98	13.57	14.13	
HCHO (mM)						

Table S6. Performance (Faradaic efficiency, cell voltage, H_2:CO ratio) of the BCE-OER (anolyte: 1 M KOH) and the BCE-FOR (anolyte: 1 M HCHO + 1 M KOH, 1 M HCHO + 2 M KOH and 2 M HCHO + 1 M KOH) using commercial BPM.

- BCE-OER

J ($mA\ cm^{-2}$)	Voltage (V)	Cathode FE CO (%)	Cathode FE H_2 (%)	Anode FE H_2 (%)	H_2:CO Ratio
100	3.53 ± 0.14	102.93 ± 1.22	0.0 ± 0.0	0.0 ± 0.0	0.0 ± 0.0
200	4.22 ± 0.13	102.19 ± 1.8	0.61 ± 1.06	0.0 ± 0.0	0.01 ± 0.01
300	5.01 ± 0.33	91.29 ± 3.39	7.47 ± 4.95	0.0 ± 0.0	0.08 ± 0.06
400	6.16 ± 0.6	75.13 ± 4.51	20.53 ± 5.39	0.0 ± 0.0	0.28 ± 0.9
500	7.71 ± 1.05	64.34 ± 4.65	34.45 ± 4.41	0.0 ± 0.0	0.54 ± 0.11
600	9.54 ± 1.21	52.02 ± 2.23	48.37 ± 3.19	0.0 ± 0.0	0.93 ± 0.08

- BCE-FOR (1 M HCHO + 1 M KOH)

J ($mA\ cm^{-2}$)	Voltage (V)	Cathode FE CO (%)	Cathode FE H_2 (%)	Anode FE H_2 (%)	H_2:CO Ratio
100	1.81 ± 0.26	97.12 ± 2.94	0.0 ± 0.0	97.84 ± 5.13	1.01 ± 0.08
200	2.59 ± 0.38	101.56 ± 3.17	0.0 ± 0.0	100.75 ± 2.62	0.99 ± 0.01
300	3.61 ± 0.43	94.76 ± 4.08	5.81 ± 0.71	102.1 ± 2.85	1.14 ± 0.08
400	4.88 ± 0.56	79.16 ± 3.32	15.77 ± 3.64	94.37 ± 2.45	1.39 ± 0.08
500	6.75 ± 0.81	70.45 ± 5.92	27.56 ± 4.05	85.38 ± 7.29	1.62 ± 0.29
600	9.46 ± 1.39	55.28 ± 6.61	43.65 ± 3.96	70.9 ± 6.23	2.1 ± 0.41

- BCE-FOR (1 M HCHO + 2 M KOH)

J ($mA\ cm^{-2}$)	Voltage (V)	Cathode FE CO (%)	Cathode FE H_2 (%)	Anode FE H_2 (%)	H_2:CO Ratio
100	1.68 ± 0.2	98.36 ± 5.72	0.0 ± 0.0	99.26 ± 2.41	1.01 ± 0.04
200	2.48 ± 0.27	100.45 ± 4.18	0.0 ± 0.0	104.85 ± 3.0	1.05 ± 0.06
300	3.45 ± 0.45	93.71 ± 2.38	2.6 ± 0.45	106.34 ± 3.26	1.16 ± 0.02
400	4.85 ± 0.82	78.96 ± 5.91	19.64 ± 9.96	102.22 ± 1.91	1.56 ± 0.27
500	6.84 ± 1.41	67.72 ± 3.86	32.2 ± 7.49	100.83 ± 4.69	1.98 ± 0.29
600	10.51 ± 2.47	54.64 ± 4.89	45.73 ± 1.8	97.92 ± 2.17	2.65 ± 0.29

- BCE-FOR (2 M HCHO + 1 M KOH)

J ($mA\ cm^{-2}$)	Voltage (V)	Cathode FE CO (%)	Cathode FE H_2 (%)	Anode FE H_2 (%)	H_2:CO Ratio
100	2.09 ± 0.24	97.75 ± 1.3	0.0 ± 0.0	104.14 ± 2.36	1.07 ± 0.04
200	3.01 ± 0.26	95.68 ± 1.21	0.53 ± 0.92	100.56 ± 8.54	1.06 ± 0.1
300	4.24 ± 0.38	94.55 ± 0.89	3.59 ± 2.07	100.01 ± 2.47	1.1 ± 0.04
400	5.96 ± 0.61	83.03 ± 2.9	13.32 ± 1.84	89.06 ± 3.08	1.24 ± 0.1
500	8.43 ± 1.27	72.23 ± 5.15	26.21 ± 3.04	79.5 ± 0.44	1.47 ± 0.16
600	13.47 ± 2.51	59.39 ± 7.16	42.65 ± 6.23	69.51 ± 11.12	1.91 ± 0.26

Supplementary Text 1

Tafel Slope Analysis for Formaldehyde Oxidation with Varying Concentrations of KOH and Formaldehyde

Table S7. Tafel slopes for formaldehyde oxidation reaction at various KOH and formaldehyde concentrations. Tafel slope values are extracted from the current density ranges from 1 to 5 mA cm^{-2}.

KOH (mM)	HCHO (mM)	Tafel slope (mV dec^{-1})
50	50	34
	100	30.7
	200	30
	500	N/A
	1000	N/A
100	50	26.69
	100	32.29
	200	30.7
	500	N/A
	1000	N/A
500	50	22.8
	100	29.15
	200	18
	500	26.6
	1000	46
1000	50	20.68
	100	19.79
	200	27.2
	500	33.91
	1000	27.15
2000	50	23.34
	100	27.41
	200	21.25
	500	19.78
	1000	24.75

To gain insight into the reaction mechanism of the formaldehyde oxidation reaction (FOR), we performed Tafel slope analysis under varying KOH and HCHO concentrations. Tafel slopes were extracted in the low current density regime (less than 10 mA cm^{-2}), where kinetic control is expected with 100% ohmic resistance compensation.[19] This range minimizes mass transport contributions that could obscure identification of kinetically relevant steps. Across all tested conditions, including varying ratios of KOH (50 mM to 2000 mM) and HCHO (50 mM to 1000 mM), the Tafel slopes consistently ranged from 19 to 46 mV dec^{-1}, with most values centered around 20–30 mV dec^{-1}. These values are significantly lower than the expected 40 or 120 mV dec^{-1} associated with one-electron transfer-limited steps in alkaline electrocatalysis.[20] Thus, we suggest that the rate-determining process does not primarily involve a charge-transfer step.

Importantly, previous mechanistic studies of aldehyde oxidation on Cu-based catalysts have identified surface hydrogen recombination pathways through operando and theoretical analyses. For example, operando DEMS measurements and DFT calculations demonstrated that hydrogen generated from C–H cleavage of aldehyde can undergo recombination under low overpotential conditions rather than Volmer-type oxidation to H_2O.[1] Likewise, in-situ and DFT investigations suggested that while C–H cleavage is facilitated on mixed Cu surfaces, the subsequent H–H bond formation step may present a higher energetic barrier depending on surface structure.[21] In this context, the low Tafel slopes observed here are consistent with a regime in which non-electron-transfer surface processes involving adsorbed hydrogen species contribute to the kinetics.

We therefore suggest that the observed kinetics may be influenced by surface hydrogen recombination ($*H + *H \rightarrow H_2$), also known as the Tafel step (30 mV dec^{-1}). Additionally, the slightly lower Tafel slopes or higher slopes than the classical 30 mV dec^{-1} for the Tafel step may reflect variations in hydrogen coverage, surface states, or local catalytic environments that can influence the apparent kinetic step.[22] However, we emphasize that our analysis provides indirect kinetic evidence rather than direct spectroscopic confirmation of this pathway. Moreover, a range of Tafel slopes (20–50 mV dec^{-1}) has been reported in related aldehyde and biomass electrooxidation systems, underscoring that similar apparent values can arise from different mechanistic scenarios.[23-25] Therefore, while the present values are kinetically consistent with a recombination-influenced regime under low-overpotential conditions, they should be interpreted within the broader context of mechanistic complexity in aldehyde electrooxidation.

Reaction Order Analysis for Formaldehyde Oxidation with Varying Concentrations of Formaldehyde

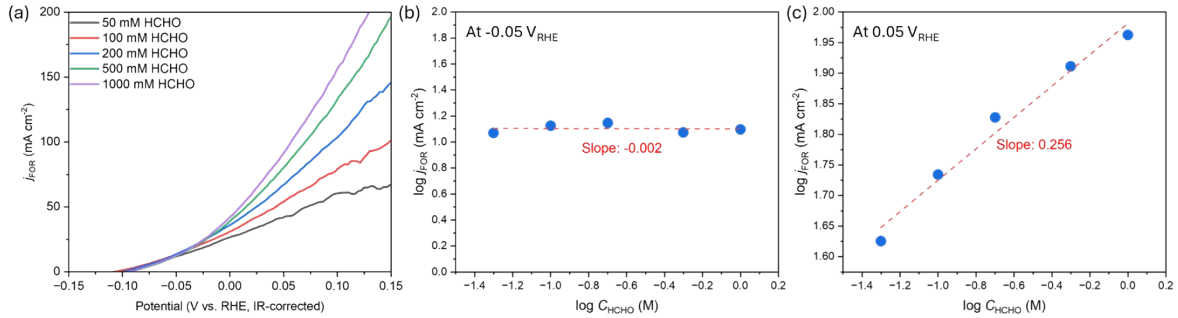

Fig. S26. (A) Formaldehyde oxidation current densities at varying formaldehyde concentrations under fixed KOH concentration (2000 mM). Double-logarithmic plots of current density as a function of formaldehyde concentration at (b) -0.05 V_{RHE} and (c) 0.05 V_{RHE}. The slopes of the linear fits correspond to the apparent reaction order with respect to formaldehyde under the indicated potentials.

We analyzed the reaction order with respect to formaldehyde concentration to further probe this interpretation (**Fig. S26**). In the low overpotential region corresponding to the Tafel analysis (where mass transport effects are minimal, at -0.05 V_{RHE}), the reaction order with respect to formaldehyde concentration showed approximately zero. This weak dependence on formaldehyde concentration suggests that the kinetically relevant step in this regime does not directly involve formaldehyde adsorption or C–H bond cleavage, and is consistent with a surface hydrogen recombination-limited process. In this case, rapid formaldehyde activation and H* formation relative to the recombination step could lead to a quasi-saturated hydrogen coverage, thereby decoupling the observed rate from bulk formaldehyde concentration. A similar apparent zero-order behavior arising from surface intermediate saturation has been reported in electrochemical CO reduction systems, where CO–CO coupling remains rate-determining despite nCO approaching zero at high CO pressures.[26,27] Interestingly, at higher overpotential (0.05 V_{RHE}), the reaction order with the respect to formaldehyde concentration increases (~0.256), indicating a growing influence of formaldehyde concentration on the observed rate. This transition suggests that the rate-determining step may shift as the potential increases, potentially involving earlier surface processes such as C–H bond activation under more strongly driven conditions. Taken together, the combined Tafel slope and reaction order analyses suggest that the dominant kinetic bottleneck may

vary with applied potential. Under low overpotential conditions, the kinetics are consistent with a non-electron transfer surface step involving hydrogen recombination, whereas at higher overpotentials, formaldehyde-related surface reactions may become increasingly rate-influencing.

Supplementary Text 2

Bicarbonate Electrolysis for Direct Conversion of Carbon Capture Solutions.

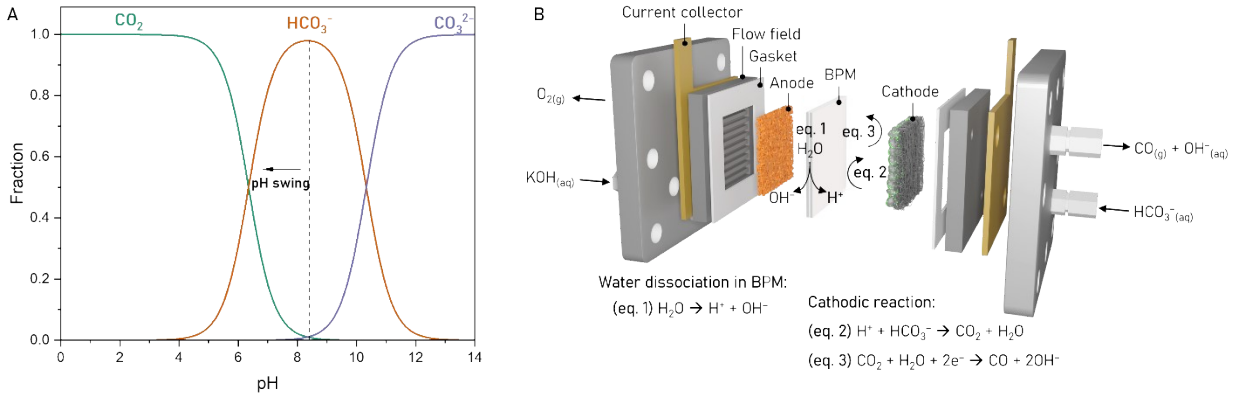

Fig. S27. Equilibrium reaction-based bicarbonate electrolysis system. (A) Equilibrium distribution of CO_2, HCO_3^-, and CO_3^{2-} species as a function of pH. The dotted vertical line indicates the pH of 3 M $KHCO_3$ solution. The pH swing induced by the BPM shifts the CO_2/HCO_3^- equilibrium toward CO_2 generation, facilitating *in-situ* CO_2 release from bicarbonate near the catalyst surface. (B) Detailed mechanisms of bicarbonate electrolysis in a BPM-MEA system.

$$H_2O \rightarrow H^+ + OH^- \text{ (BPM under reverse bias)} \qquad \text{(eq. 1)}$$

$$H^+ + HCO_3^- \rightarrow CO_2 + H_2O \text{ (pH swing near BPM-cathode interface)} \qquad \text{(eq. 2)}$$

$$CO_2 + H_2O + 2e^- \rightarrow CO + 2OH^- \text{ (CO_2 reduction at cathode)} \qquad \text{(eq. 3)}$$

$$H_2O + 2e^- \rightarrow 1/2H_2 + 2OH^- \text{ (H_2 evolution reaction at cathode)} \qquad \text{(eq. 4)}$$

Bicarbonate electrolysis (BCE) has recently emerged as a promising strategy for CO_2 reduction reaction (CO_2RR), particularly due to its compatibility with upstream carbon capture processes. Unlike conventional CO_2 electrolysis systems that require high-purity gaseous CO_2 which often involves energy-intensive pressurization, purification, and storage steps, BCE enables direct conversion of captured CO_2 in the form of bicarbonate or carbonate solutions.

Alkaline capture solutions, such as bicarbonates or carbonates, are commonly used in direct air capture (DAC) and flue gas absorption. In BCE, these bicarbonate-rich electrolytes can be directly fed into the catholyte. However, since bicarbonate solutions are electrochemically inert, an additional acidification step is required to generate reactive carbon species (aqueous or gas-

phase CO_2). The equilibrium between CO_2, HCO_3^-, and CO_3^{2-} is highly pH-dependent, with increased acidity promoting CO_2 release from bicarbonate (**Fig. S27A**). At lower pH of the bicarbonate solution, the equilibrium between CO_2 and HCO_3^- shifts toward CO_2 evolution. To induce pH swing near the cathode, a bipolar membrane (BPM) is employed in the BCE system (**Fig. S27B**). Under reverse bias operation of the BPM, water dissociation at the junction generates H^+ at cathode and OH^- at anode (**eq. 1**). The locally acidic environment at the interface between the BPM and the electrode facilitates the *in-situ* generation of CO_2 from bicarbonates (**eq. 2**), enabling the CO_2RR. Despite the locally acidic conditions created by the BPM near the electrode, the bulk pH of the bicarbonate solution tends to increase over time due to the generation of OH^- as a byproduct of both CO_2RR and the hydrogen evolution reaction (HER) during electrolysis (**eqs. 3 and 4**). As the pH gradually increases, the in-situ generation of CO_2 is hindered, leading to a decline in CO_2RR activity. To mitigate this issue, we integrated a carbon capture process by continuously bubbling CO_2 into the bicarbonate solution (**Fig. S4**). The continuous supply of CO_2 converts OH^- back into bicarbonate, thereby maintaining the bicarbonate concentration.[9] This process enables the system to operate under pseudo-steady-state conditions during electrolysis.

.

Supplementary Text 3

Systematic Evaluation of Anodic Side Reactions

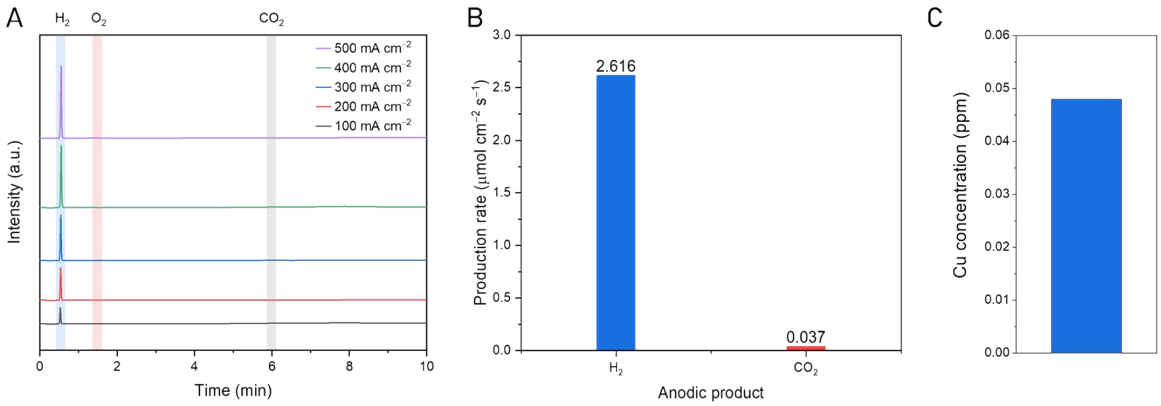

Fig. S28. **Systematic evaluation of anodic side reactions and catalyst stability.** (a) on-line GC analysis of the anode outlet. The direct gas-phase analysis confirms the absence of O_2 and CO_2 gas evolution in the highly alkaline environment (2 M KOH + 1 M HCHO). (b) quantification of dissolved carbonates via acidification-coupled GC. The post-reaction electrolyte was injected into a 1 M HCl solution to release dissolved carbonates as CO_2 gas, revealing a practically negligible deep oxidation rate. (c) ICP-OES analysis. The concentration of dissolved Cu in the electrolyte was measured after 30 min of electrolysis at 600 mA cm^{-2}, confirming strictly negligible anodic dissolution.

To comprehensively evaluate the anodic side reactions during the FOR, we systematically investigated the degree of deep oxidation to CO_2 and the structural stability of the Cu anode. In a highly alkaline environment (2 M KOH), any CO_2 generated from deep oxidation is immediately captured as dissolved carbonate (CO_3^{2-}). Therefore, direct gas-phase detection at the anode outlet inherently yields no CO_2 signals (**Fig. S28A**). To accurately quantify the dissolved CO_2 products, we designed an acidification experiment. The post-reaction electrolyte, which had been operated with 2 M KOH and 1 M HCHO at 500 mA cm^{-2}, was continuously injected into a strong acid solution (1 M HCl) to shift the chemical equilibrium and release all dissolved carbonates as CO_2 gas. Subsequent real-time quantification using GC revealed a CO_2 production rate of 0.037 μmol cm^{-2} s^{-1} (**Fig. S28B**). To evaluate the impact of this deep oxidation on the overall charge consumption, we calculated the FE. Deep oxidation to CO_2 could theoretically originate from

multiple reaction pathways. Based on the standard thermodynamic potentials (vs. RHE) for catalytic CO_2 interconversion, the relevant anodic pathways are described as follows[28,29]:

$$CH_3OH + H_2O \rightarrow CO_2 + 6H^+ + 6e^- \quad (E^o = 0.03\ V) \quad \text{(eq. 5)}$$

$$HCHO + H_2O \rightarrow CO_2 + 4H^+ + 4e^- \quad (E^o = 0.07\ V) \quad \text{(eq. 6)}$$

$$HCOO^- + 3OH^- \rightarrow CO^{2-}_3 + 2H_2O + 2e^- \quad (E^o = -0.22\ V) \quad \text{(eq. 7)}$$

At an applied current density of 500 mA cm^{-2}, the FE for CO_2 production depends on the electron demand of the specific pathway. In the optimal scenario where CO_2 originates from formate oxidation (the $2e^-$ pathway), the FE is calculated to be merely ~1.4%. Even assuming the worst-case scenario with the maximum electron demand (the $6e^-$ pathway from methanol), the FE for CO_2 production is bounded at a low value of ~4.3%. These quantitative results confirm that while the deep oxidation of HCHO does occur as a minor parasitic pathway, its contribution to the overall parasitic charge consumption is practically negligible, ensuring that the vast majority of the applied current drives the targeted FOR process.

Finally, to address the possibility of Cu dissolution under these highly alkaline anodic conditions, we analyzed the electrolyte using ICP-OES. After operating the electrolysis cell at a high current density of 600 mA cm^{-2} for 30 min, the concentration of dissolved Cu in the electrolyte was found to be merely 0.048 ppm, whereas no Cu was detected prior to the reaction (**Fig. S28C**). This negligible trace amount confirms that the anodic dissolution of the Cu catalyst is strictly limited. This observation is also highly consistent with our stability test (**Fig. S22**), indicating that the Cu electrocatalyst maintains robust structural integrity without significant metal leaching during operation.

Supplementary Text 4

Thermodynamic Speciation Analysis of Formaldehyde

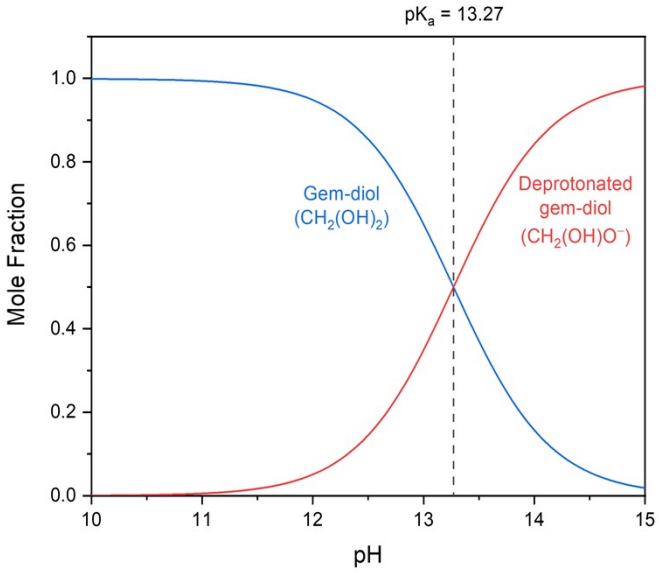

Fig. S29. Thermodynamic speciation analysis of formaldehyde

To elucidate the mechanism behind the enhanced FOR activity at high KOH concentrations, we performed a thermodynamic speciation analysis of formaldehyde in aqueous alkaline solutions. In aqueous environments, formaldehyde (HCHO) undergoes a rapid hydration reaction to form gem-diol ($CH_2(OH)_2$), as described by Eq. 8:

$$HCHO + H_2O \rightleftharpoons CH_2(OH)_2 \qquad \text{(eq. 8)}$$

The hydration equilibrium constant (K_{hyd}) is defined as:

$$K_{hyd} = \frac{[CH_2(OH)_2]}{[HCHO]} \qquad \text{(eq. 9)}$$

K_{hyd} of the HCHO is approximately 1,270 at 298.15 K.[30] This large equilibrium constant indicates that free HCHO is virtually non-existent in the solution (>99.9% exists as the gem-diol form), making gem-diol the primary reactant reservoir. Under highly alkaline conditions, the gem-diol acts as a weak acid and undergoes deprotonation to form the gem-diolate mono-anion

($CH_2(OH)O^-$), which is considered the key active electroactive species for the FOR on copper electrodes:

$$CH_2(OH)_2 \rightleftharpoons CH_2(OH)O^- + H^+ \quad \text{(eq. 10)}$$

The acid dissociation constant (K_a) for this deprotonation step is given by:

$$K_a = \frac{[CH_2(OH)O^-][H^+]}{[CH_2(OH)_2]} \quad \text{(eq. 11)}$$

The pK_a of gem-diol is accurately determined to be 13.27 at 25 °C.[31] Based on these thermodynamic constants (K_{hyd} =1270 and pK_a =13.27), the mole fractions (α) of the gem-diol and the deprotonated gem-diol species as a function of pH can be calculated using the following mass balance equations:

$$\alpha_{gem-diol} = \frac{1}{1 + \frac{1}{K_{hyd}} + 10^{(pH - pK_a)}} \quad \text{(eq. 12)}$$

$$\alpha_{deprotonated\ gem-diol} = \frac{10^{(pH - pK_a)}}{1 + \frac{1}{K_{hyd}} + 10^{(pH - pK_a)}} \quad \text{(eq. 13)}$$

Fig. S29 shows the resulting speciation plot. As the pH approaches and exceeds the pK_a value of 13.27 (e.g., in highly concentrated KOH solutions), the equilibrium sharply shifts toward the formation of the deprotonated gem-diol. The fraction of this active intermediate approaches unity at pH > 14.

This thermodynamic trend provides strong theoretical support for our experimental observation (the competition between FOR and the Cannizzaro reaction), confirming that the increase in KOH concentration drastically increases the availability of the active deprotonated gem-diol, thereby accelerating the electrochemical oxidation kinetics before the parasitic Cannizzaro reaction eventually dominates at excessive alkalinity.

Supplementary Text 5
Synthetic Bipolar Membrane (s-BPM) Characterizations.

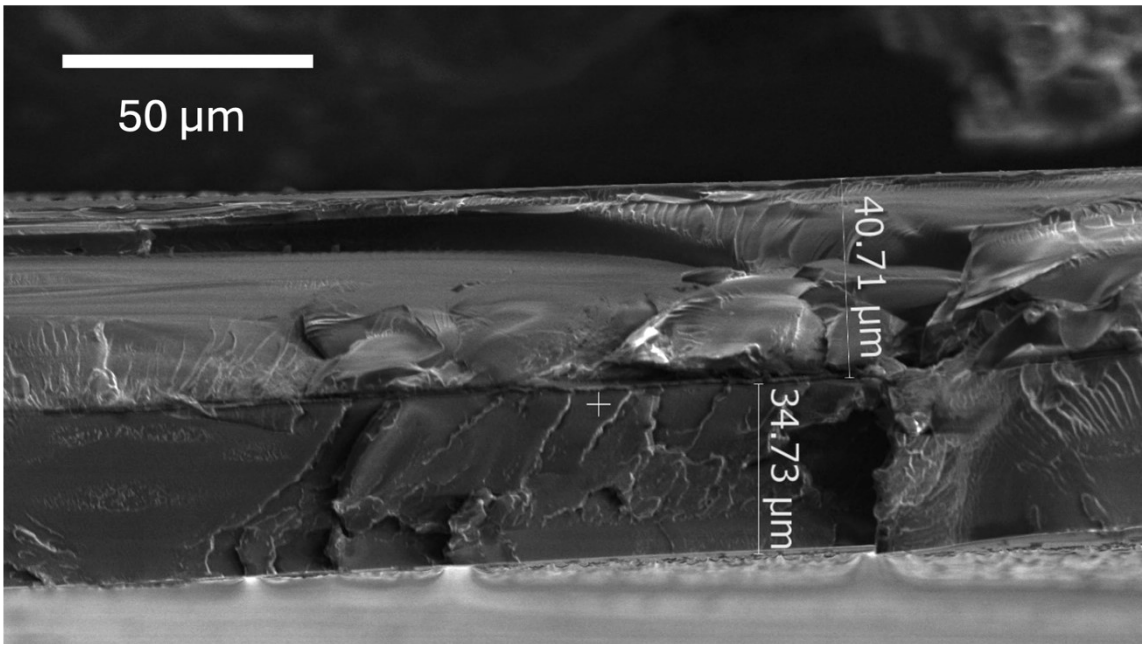

Fig. S30. Cross-sectional SEM image of the s-BPM. The s-BPM is composed of a cation-exchange membrane (CEM, top) and an anion-exchange membrane (AEM, bottom). The catalyst layer is extremely thin and not visible in the SEM image.

The s-BPM consists of a cation-exchange membrane (CEM) layered atop an anion-exchange membrane (AEM), as shown in the cross-sectional SEM image (**Fig. S30**). A thin catalyst interlayer (SnO_2) was incorporated at the junction to potentially assist water dissociation by aligning water molecules under the interfacial electric field,[2] however, this layer is too thin to be resolved in the SEM image. Both the CEM and AEM are fabricated from high-conductivity ionomers originally developed for fuel cell applications. While these polymers exhibit relatively low permselectivity, the outward flux of H^+ and OH^- from the junction is hypothesized to help suppress the crossover of undesired counter-ions.[32,33] In contrast to the c-BPM, which typically employ thick ion-exchange layers (180 – 200 µm total), the s-BPM utilizes substantially thinner polymer layers (~ 80 µm total) to reduce ohmic losses and enhance ion transport efficiency.

Supplementary Text 6
Process Energy Analysis.

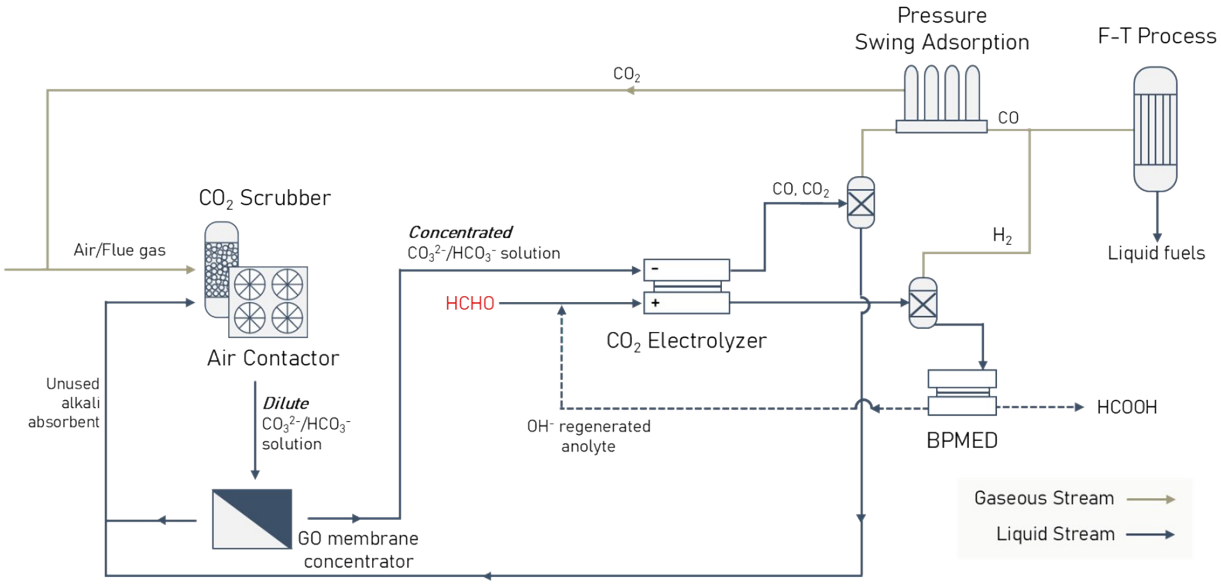

Fig. S31. Process flow diagram for the BCE-FOR w/ s-BPM electrolysis. The key process units include the scrubbers for carbon capture, membranes for carbonate concentration, the electrolyzer to produce syngas, formates, downstream separation units and finally the Fischer-Tropsch reactor to produce liquid fuels. BPMED refers to bipolar membrane electrodialysis unit for recovering the formates as formic acid and regenerating the anolyte.

The modelling framework used for this work is built on our previous work,[34] the key assumptions are summarized here. A full process schematic is shown in **Fig. S31**. It begins with the capture of CO_2 from concentrated sources such as flue gas is preferred over direct air capture for this application due to the requirement of (i) concentrated bicarbonate solution as feed to the electrolyzer and (ii) drastically low energy requirement to capture one unit mass of CO_2. The absorbent would be 0.6–1 M KOH and carried out using a CO_2 scrubber and the regeneration of the absorbent occurs in the cathode of the liquid phase electrolyzer.[35] However, in case of the gas-fed AEM electrolyzers, the need for the energy intensive stripping operation to recover gaseous CO_2 at high purity to much higher levelized energy requirement over the former case to produce bicarbonates. For the conventional amine-based absorption process, 370 kWh t_{CO2}^{-1},[36] is required. Direct estimates for alkali based capture from a concentrated flue gas are not readily available in the literature, however for direct air capture 1338 kWh t_{CO2}^{-1} [9] is required. Following this, the stream is concentrated to the desired level using a graphene oxide-based membrane which offers

stable operation at high temperature and high pH environments. Typically, the bicarbonate concentration from the alkali-based flue gas scrubber could be as low as 0.6 M against the desired 3 M for BCE-FOR.[37] The use of multi-effect evaporators for concentration processes is often limited by their high thermal energy requirements. As a more energy-efficient alternative, membrane-based separation has gained attention. In this context, the use of graphene oxide membrane technology for such applications has enabled a substantial reduction in thermal energy consumption.[34] However, this approach necessitates fluid pumping at elevated pressures (approximately 50 bar), thereby shifting a portion of the energy demand from heating to mechanical work. A trade-off occurs based on the capital expenditure (CAPEX) and operational expenditure (OPEX) to identify the optimal concentration of the bicarbonate stream exiting the CO_2 capture unit to be subsequently concentrated in the membrane separation unit. The total energy for capturing and conditioning the bicarbonate stream to the desired concentration is varied between 0 and 2000 kWh t_{CO2}^{-1} captured, to allow for exigencies during scaled-up deployment of these technologies.

Downstream of the electrolyzer, there are two separation configurations, one each for the cathode and anode. For the anode, the recovery of formate entails a BPM electrodialysis (BPMED) unit as mentioned in the main text. BPMED offers an energy-efficient route for recovering formates as (dilute, ~1 M) formic acid by enabling in situ acid-base splitting through water dissociation at the bipolar membrane interface.[38] This eliminates the need for thermal energy input, which is typically required in conventional separation processes. The electrochemical driving force allows for selective transport of formate ions into the acid compartment, where they combine with protons to form formic acid. Recent studies have demonstrated that BPMED can achieve high current efficiencies and low specific energy consumption, particularly when operated in multistage configurations that enhance product concentration and purity.[39] The energy intensity of generating formic acid has been estimated to be 2600 kWh $ton_{formic\ acid}^{-1}$ [40] although this is highly dependent on the concentration of the formate ions in the anode outlet streams. This is applicable to the cathode product stream wherein the separation performance is highly dependent on the feed concentration. For the cathode, a condensate separator to recover the entrained water would be required following which the unreacted CO_2 needs to be recovered. While absorption-based methods for CO_2 recovery[41] are unsuitable under the low-pressure conditions considered here, PSA remains a commercially mature alternative widely used in conventional petrochemical

processes. The energy demand for CO_2 separation via PSA has been reported to be approximately 308 kWh per ton of feed mixture.[42] To account for uncertainties that may arise during scale-up, the net energy requirement for downstream processing and separation has been conservatively estimated to range between 0 and 4000 kWh per ton of syngas. The energy requirements for electrolyzers with different configurations are shown in **Fig. S24**. The substantial reduction observed in the BCE-FOR system w/ s-BPM is attributed to two key modifications: 1) replacement of the conventional OER with FOR at the anode, and 2) substitution of the c-BPM with the s-BPM used in this study. These changes enable a ~45% decrease in electrolyzer energy consumption compared to the gaseous CO_2 AEM configuration (CO_2E-OER w/ c-AEM). It should be noted that, in addition to the electrolysis, upstream and downstream processes also requires energy input.[34]

1. Conversion of the captured bicarbonate in the carbon capture unit into gaseous CO_2.
2. Implementation of an additional pressure swing adsorption (PSA) unit to purify the anode product stream and recover CO_2 that has crossed over through the AEM.
3. Possible electrolyzer flushing due to the deposition of (bi)carbonate salts.
4. Integration of an additional proton exchange membrane (PEM) electrolyzer to produce hydrogen, as CO Faradaic efficiency typically exceeds 90% in gas-fed electrolyzers, resulting in an unfavorable (very low) H_2:CO ratio.

In the FOR-coupled configuration, the calculated E_{cell} is positive (+0.11 V), in contrast to conventional OER-coupled CO_2 electrolysis where $E_{\text{cell}} < 0$ and an external voltage is thermodynamically required to drive the CO production as shown in supplementary **Fig. S1**. A positive E_{cell} indicates that the overall coupled reaction is spontaneous ($\Delta G < 0$) and is therefore galvanic in character, i.e., the chemical free energy released by oxidation of the organic anolyte can, in principle, drive CO_2 reduction without external electricity input. Nevertheless, despite this favorable thermodynamic directionality, the practical current density and syngas production rate remain limited by kinetic and transport losses (activation, ohmic, and mass-transfer), which can consume the available driving force and necessitate applied voltage to achieve industrially relevant operation. The favorable thermodynamics associated with a positive E_{cell} is reflected in the shaded portion of the levelized energy diagram, which represents a reduction in the required external electrical energy input relative to an OER-coupled electrolyzer. Importantly, this shading does not

imply “negative energy” or guaranteed net electricity export; rather, it indicates that part of the electrical driving force is effectively supplied by the chemical free energy of the anodic organic reactant. In other words, the metric reported in **Fig. S24** is the net electricity required from an external power source, and the shaded region should be interpreted as an offset to purchased electricity, not as a negative levelized energy requirement.

Techno-economic analysis methodology

CO_2 is captured from flue gas in a conventional counter-current gas–liquid absorber using circulating KOH solution, producing potassium carbonate. The absorber is costed as an installed “system” consistent with the NETL solvent-DAC case study, which reports a dedicated line item for the flue-gas CO_2 absorber package (“15.9 CO_2 Absorber System”) with a total plant cost of 52,293 (2020 $/1,000), i.e., 52.293 MUSD (2020 basis). NETL also provides the corresponding absorber inlet flue-gas mass flow rate of 541,000 kg/h and a flue-gas CO_2 concentration of 5.2 wt%. In this TEA, the flue-gas mass flow rate required to supply a target CO_2 capture rate is estimated from the mass fraction of CO_2 in flue gas. Let $\dot{n}_{CO_2,cap}$ denote the required CO_2 capture rate entering the absorber (kmol/s), and let $w_{CO_2,fg} = 0.052$ be the CO_2 mass fraction in flue gas, with $MW_{CO_2} = 44$ kg/kmol. The corresponding flue-gas mass flow is computed as

$$\dot{m}_{fg} = \frac{\dot{n}_{CO_2,cap}\, MW_{CO_2}}{w_{CO_2,fg}}$$

For scaling, the NETL reference flue-gas mass flow is $\dot{m}_{fg,ref} = 541{,}000/3600 = 150.28$ kg/s.

The installed absorber CAPEX is obtained by scaling the NETL “CO_2 Absorber System” cost with a 0.7 capacity exponent, consistent with NETL’s scaling guidance for this account (gas-flow-based scaling). The resulting fixed-capital investment for the absorber system is

$$FCIL_{CCU} = (52.293 \times 10^6)\left(\frac{\dot{m}_{fg}}{\dot{m}_{fg,ref}}\right)^{0.7} f_{cap}$$

where f_{cap} is a dimensionless CAPEX multiplier used for sensitivity analysis.

Annual electricity cost for the absorber system is computed from a reference electric load scaled linearly with flue-gas flow. NETL reports an absorber flue-gas blower auxiliary load of 1,490 kWe and reports "KOH pumps" as an auxiliary-load category of 8,970 kW; in the conservative allocation used here these are combined to define a reference load $P_{ref} = 10{,}460$ kWe for the capture block. Annual electricity cost is then calculated as

$$CUT_{CCU} = \frac{SF \cdot 8760 \cdot P_{ref} \cdot \left(\frac{\dot{m}_{fg}}{\dot{m}_{fg,ref}}\right) \cdot c_e}{10^6}$$

reported in MUS$/yr, where SF is the stream factor and c_e is the electricity price ($/kWh). A sample calculation follows directly from the above expressions. Given a model-computed $\dot{n}_{CO_2,cap}$ (kmol/s), the flue-gas mass flow is first obtained from $\dot{m}_{fg} = \dot{n}_{CO_2,cap}(44/0.052)$.

The carbonate concentration step is modeled as a membrane-based concentrator sized from the required water permeation to reach a target carbonate molarity in the retained stream. The mass balances and scaling logic follow the integrated capture-to-conversion process framework and TEA conventions used by Venkataraman et al.[34] for alkaline-carbonate process designs, including recycling and concentration of capture solutions prior to electrochemical conversion. In the model, membrane area is calculated from a permeance relation with an assumed transmembrane pressure (TMP), and capital cost is computed from an area-based cost correlation with a scale exponent. In equation form, the membrane area is obtained as

$$A_{GO} = \frac{\dot{m}_{perm}}{\Pi_w \, \Delta P} 3600$$

where $\dot{m}_{perm}$ is the permeating water mass flow (kg/s), Π_w is the water permeance (in the same units used in your code), and ΔP is TMP. Installed CAPEX is then represented as

$$FCIL_{GO} = C_m (A_{GO})^{0.85} f_{inst}$$

where C_m is the membrane-cost coefficient and f_{inst} is your installation multiplier. A sample calculation is performed by substituting your computed $\dot{m}_{perm}$, the chosen TMP (e.g., 50 bar in your script), and the permeance parameter into the area expression, then evaluating $FCIL_{GO}$ from the cost correlation.

Electrolyzer sizing and costing are based on the standard current-based TEA framework for carbonate electrolysis systems, consistent with the integrated process modeling and cost structure in Venkataraman et al.[34] The total current required for a specified CO production rate is computed from Faraday's law using the electron stoichiometry for CO formation ($n_{CO} = 2$), a specified Faradaic efficiency to CO, and the plant stream factor:

$$I_{tot} = \frac{\dot{n}_{CO}\, n_{CO} F}{FE_{CO}\, SF}$$

The geometric electrode area is then

$$A_{elec} = \frac{I_{tot}}{j}$$

where j is current density. Electrical power is computed as

$$P = \frac{I_{tot} V}{1000}$$

with P in kW when I is in A and V in V. Stack count follows from an assumed active area per cell and cells per stack, and stack CAPEX is obtained by summing area-scaled component costs multiplied by a stack-cost factor and an installation multiplier, following the same kind of bottom-up stack accounting used in Venkataraman et al.[34] A sample calculation is obtained by inserting $\dot{n}_{CO}$ (derived from your CO TPA target), FE_{CO}, j, and V to compute I_{tot}, A_{elec}, and P, then evaluating the component-based stack CAPEX. he electrolyzer fixed capital investment is calculated by summing the area-scaled costs of the major stack components (cooling plate, cathode and anode diffusion layers, bipolar membrane, MEA/frame, and bipolar plates), multiplying by the number of stacks, and applying the stack-cost multiplier and installation factors (i.e., $FCIL_{Echem} = \left[\sum_k c_k(A_{stack})\right] N_{stack}\, f_{stack}\, f_{inst}$), consistent with the bottom-up stack costing approach used in Venkataraman et al.[34]

The cathode product split is determined by Faradaic efficiencies, so the cathode H_2 rate goes to zero when $FE_{H2} = 0$ and $FE_{CO} = 1$. In contrast, the anode H_2 (from your HCHO oxidation half-reaction) is computed directly from the total current, so it remains nonzero whenever the cell

operates. With your assumption that the anode pathway uses 100% of anodic current, the anode H_2 molar rate is $\dot{n}_{H2,an} = I_{tot}/(2F)$, converted to kg/h. We assume the values of cell voltage and FEs for corresponding to the 600 mA/cm^2 for the 2:1 H_2/CO syngas from the electrolyzer and the values corresponding to the 200 mA/cm^2 for the 1:1 H_2/CO syngas from the electrolyzer with the balance being supplied by green H_2. Total electrolyzer H_2 available for downstream synthesis is then

$$\dot{m}_{H2,avail} = \dot{m}_{H_2,cath} + \dot{m}_{H_2,anode}$$

and the green H_2 makeup requirement is computed as

$$\dot{m}_{H2,makeup} = max\left(0, \dot{m}_{H2,req} - \dot{m}_{H2,avail}\right)$$ which matches the integrated material-balance logic used for capture-to-conversion process TEAs in Venkataraman et al.[34]

The BPMED unit is modeled with an active-area sizing based on charge throughput and a cost model written per unit membrane/stack area. For electrodialysis with bipolar membranes (EDBM/BPMED), Virruso et al. report and use a triplet specific cost basis (e.g., 600 US$/m²) and an explicit triplet/stack cost formulation that scales with membrane costs.[43] For membrane-price assumptions derived from suppliers, Salas et al. report representative values (e.g., BPM and IEM costs per m²) used in an economic evaluation of BMED.[44] In equation form, the required BPMED area for a target acid production rate is written as

$$A_{BPMED} = \frac{\dot{n}_{acid} F}{j_{BPMED}\, CE_{BPMED}}$$

assuming monovalent acid production (one equivalent of charge per mole acid) and a current efficiency CE_{BPMED}. The installed CAPEX is modeled as

$$FCIL_{BPMED} = A_{BPMED}\, C_{area}\, f_{inst}$$

where C_{area} is the adopted $/m² basis constructed from triplet/stack and membrane costs. The electricity OPEX is modeled using a specific electricity consumption basis:

$$CUT_{BPMED} = \frac{(kWh/kg)\, \dot{m}_{HCOOH}\, 8760\, SF\, c_e}{10^6}$$

reported in MUSD/yr. A sample calculation uses your computed formate production rate (converted to formic acid equivalent), a chosen $j_{BPMED}$and $CE_{BPMED}$to compute A_{BPMED}, then evaluates $FCIL_{BPMED}$and CUT_{BPMED}using the adopted area-cost and kWh/kg assumptions. The MSP of syngas is computed as the price of syngas for which the net present value (NPV) breaks even at the end of plant life (25 years). In this elementary techno-economic analysis, we assume that the 1 M HCOOH is sold at 0.032 US$/L[45] and the HCHO is purchased at 0.5 US$/kg[46].

Supplementary Text 7

Case 1: Using HCHO derived from natural gas

1. Steam methane reforming to syngas: $CH_4 + H_2O \rightarrow CO + 3H_2$
2. Catalytic hydrogenation to methanol: $CO + 2H_2 \rightarrow CH_3OH$
3. Partial Oxidation to formaldehyde: $CH_3OH + ½\ O_2 \rightarrow HCHO + H_2O$
4. Bicarbonate production (CO_2 capture): $CO_2 + OH^- \rightarrow HCO_3^-$
5. Electrolysis: **Cathode (BCE)*:** $HCO_3^- + H^+ \rightarrow CO_2 + H_2O$ $CO_2 + H_2O + 2e^- \rightarrow CO + 2OH^-$ **BPM:** $H_2O \rightarrow H^+ + OH^-$ **Anode (FOR):** $HCHO + 2OH^- \rightarrow ½\ H_2 + HCOO^- + H_2O + e^-$
6. BPMED (formic acid recovery): $HCOO^- + H^+ \rightarrow HCOOH$ $H_2O \rightarrow H^+ + OH^-$

Overall balance (assuming no side reactions):

$CO_2 + 2CH_4 + O_2 + H_2O \rightarrow CO + 3H_2 + 2HCOOH$

Case 2: Using HCHO derived from direct CO_2 hydrogenation (assuming policy constraints on natural gas use)

1. Catalytic CO_2 hydrogenation to methanol: $CO_2 + 3H_2 \rightarrow CH_3OH+H_2O$
2. Partial Oxidation to formaldehyde: $CH_3OH + ½\ O_2 \rightarrow HCHO + H_2O$
3. Bicarbonate production (CO_2 capture): $CO_2 + OH^- \rightarrow HCO_3^-$
4. Electrolysis: **Cathode (CO_2RR):** $HCO_3^- + H^+ \rightarrow CO_2 + H_2O$ $CO_2 + H_2O + 2e^- \rightarrow CO + 2OH^-$ **BPM:** $H_2O \rightarrow H^+ + OH^-$ **Anode (FOR):** $HCHO + 2OH^- \rightarrow ½\ H_2 + HCOO^- + H_2O + e^-$

5. BPMED (formic acid recovery):
$HCOO^- + H^+ \rightarrow HCOOH$
$H_2O \rightarrow H^+ + OH^-$

Overall balance (assuming no side reactions)**:**

$3CO_2 + O_2 + 5H_2 \rightarrow CO + 3H_2O + 2HCOOH$

Case 3: Using higher aldehydes as feedstock (using furfural as an example)

1. Pentose sugar dehydration to furfural:
$C_5H_{10}O_5 \rightarrow C_5H_4O_2 + 3H_2O$
2. Bicarbonate production (CO_2 capture):
$CO_2 + OH^- \rightarrow HCO_3^-$
3. Electrolysis: **Cathode (CO_2RR):** $HCO_3^- + H^+ \rightarrow CO_2 + H_2O$ $CO_2 + H_2O + 2e^- \rightarrow CO + 2OH^-$ **BPM:** $H_2O \rightarrow H^+ + OH^-$ **Anode (furfural oxidation reaction):** $C_5H_4O_2 + 2OH^- \rightarrow ½\ H_2 + C_5H_3O_3^- + H_2O + e^-$
4. BPMED (furoic acid recovery):
$C_5H_3O_3^- + H^+ \rightarrow C_5H_4O_3$
$H_2O \rightarrow H^+ + OH^-$

Overall balance (assuming no side reactions)**:**

$CO_2 + 2C_5H_{10}O_5 \rightarrow CO + H_2 + 5H_2O + 2C_5H_4O_3$

Supplementary Text 8

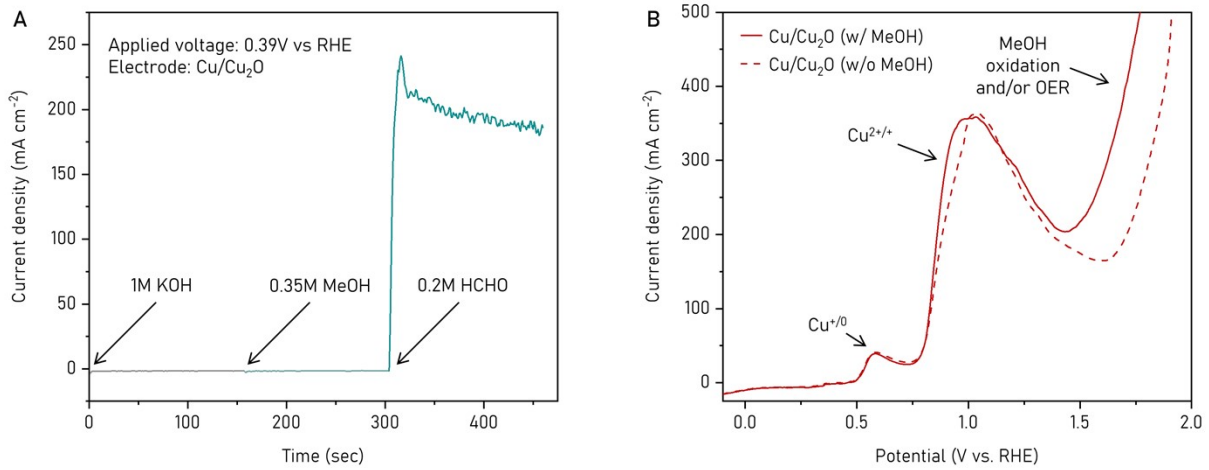

Fig. S32. Electrochemical evaluation of methanol oxidation on Cu/Cu_2O foam. (A) CA measurement at 0.39 V vs. RHE in 1 M KOH, with sequential addition methanol and formaldehyde. (B) LSV of Cu/Cu_2O in 1 M KOH with and without methanol.

Given that commercial formalin solutions typically contain methanol (10−15 wt%) as a stabilizer, it is essential to confirm that methanol oxidation does not interfere with the FOR. 1 M HCHO solution may contain approximately 0.26−0.39 M methanol; for the control experiments described below, we use the midpoint value of 0.35 M methanol to represent this background concentration. To assess this, CA was performed at a fixed potential of 0.39 V vs. RHE in 1M KOH (**Fig. S32A**). Upon injection of 0.5ml methanol (~0.35 M methanol) into the electrolyte, no significant change in current density was observed, indicating negligible catalytic activity toward methanol oxidation under these conditions. In contrast, the subsequent addition of 0.5 ml HCHO (~0.2 M HCHO) resulted in a sharp increase in current, demonstrating selective reactivity of the Cu/Cu_2O catalyst toward FOR. Further analysis using LSV (**Fig. S32B**) compared the electrochemical response of Cu/Cu_2O in 1 M KOH with and without methanol (0.35 M). A distinct increase in current density was observed only above ~1.5 V vs. RHE in the methanol-containing electrolyte, corresponding to methanol oxidation reaction and/or oxygen evolution reaction (OER). This potential region lies well beyond the operating range for FOR (**Fig. 3A**), which occurs below 0.8 V vs. RHE. Moreover, post-electrolysis characterization (**Fig. S10**) shows that no Cu^{2+} (but Cu^{+}) species are present in the XPS spectra, with no detectable oxygen species (OER product) throughout the electrolysis

process. This further suggests that methanol does not participate in the electrochemical reactions under the applied operating conditions in this work.

References

1. T. Wang, L. Tao, X. Zhu, C. Chen, W. Chen, S. Du, Y. Zhou, B. Zhou, D. Wang, C. Xie, P. Long, W. Li, Y. Wang, R. Chen, Y. Zou, X.-Z. Fu, Y. Li, X. Duan and S. Wang, *Nat. Catal.*, 2022, **5**, 66-73.
2. S. Sasmal, L. Chen, P. V. Sarma, O. T. Vulpin, C. R. Simons, K. M. Wells, R. J. Spontak and S. W. Boettcher, *Nat. Mater.*, 2024, **23**, 1421-1427.
3. Y. Zheng, N. Hu, H. Wang, N. Bu, F. Zhang and R. Zhou, *J. Membr. Sci.*, 2015, **475**, 303-310.
4. Z. Zhang, E. W. Lees, S. Ren, B. A. W. Mowbray, A. Huang and C. P. Berlinguette, *ACS Cent. Sci.*, 2022, **8**, 749-755.
5. Y. C. Xiao, C. M. Gabardo, S. Liu, G. Lee, Y. Zhao, C. P. O'Brien, R. K. Miao, Y. Xu, J. P. Edwards, M. Fan, J. E. Huang, J. Li, P. Papangelakis, T. Alkayyali, A. Sedighian Rasouli, J. Zhang, E. H. Sargent and D. Sinton, *EES catal.*, 2023, **1**, 54-61.
6. G. Lee, Y. C. Li, J.-Y. Kim, T. Peng, D.-H. Nam, A. Sedighian Rasouli, F. Li, M. Luo, A. H. Ip, Y.-C. Joo and E. H. Sargent, *Nat. Energy*, 2021, **6**, 46-53.
7. M. Shen, L. Ji, D. Cheng, Z. Wang, Q. Xue, S. Feng, Y. Luo, S. Chen, J. Wang, H. Zheng, X. Wang, P. Sautet and J. Zhu, *Joule*, 2024, **8**, 1999-2015.
8. X. Lu, C. Zhou, R. S. Delima, E. W. Lees, A. Soni, D. J. Dvorak, S. Ren, T. Ji, A. Bahi, F. Ko and C. P. Berlinguette, *Nat. Chem.*, 2024, **16**, 979-987.
9. H. Song, C. A. Fernández, H. Choi, P.-W. Huang, J. Oh and M. C. Hatzell, *Energy Environ. Sci.*, 2024, **17**, 3570-3579.
10. Z. Zhang, E. W. Lees, F. Habibzadeh, D. A. Salvatore, S. Ren, G. L. Simpson, D. G. Wheeler, A. Liu and C. P. Berlinguette, *Energy Environ. Sci.*, 2022, **15**, 705-713.
11. Y. C. Li, G. Lee, T. Yuan, Y. Wang, D.-H. Nam, Z. Wang, F. P. García de Arquer, Y. Lum, C.-T. Dinh, O. Voznyy and E. H. Sargent, *ACS Energy Lett.*, 2019, **4**, 1427-1431.
12. B. Zhou, H. Liu, G. Su, H. Shin, X.-Y. Li, H. Ze, Y. Liang, B. Peng, W. Ni, Y. Chen, W. Zhu, C. Yu, Y. Chen, P. Ou, K. Xie and E. H. Sargent, *Joule*, 2025, **9**.
13. P. Yue, K. Xiong, L. Ma, J. Li, L. Zhang, X. Zhu, Q. Fu and Q. Liao, *ACS Appl. Mater. Interfaces.*, 2022, **14**, 54840-54847.
14. J. H. Kim, H. Jang, G. Bak, W. Choi, H. Yun, E. Lee, D. Kim, J. Kim, S. Y. Lee and Y. J. Hwang, *Energy Environ. Sci.*, 2022, **15**, 4301-4312.
15. D. He, X. Ma, H. Zhou, Y. Zhang and Y. Wu, *Joule*, 2025, **9**, 101806.
16. K. M. G. Langie, K. Tak, C. Kim, H. W. Lee, K. Park, D. Kim, W. Jung, C. W. Lee, H.-S. Oh, D. K. Lee, J. H. Koh, B. K. Min, D. H. Won and U. Lee, *Nat. Commun.*, 2022, **13**, 7482.
17. Y. Kim, E. W. Lees, C. Donde, A. M. L. Jewlal, C. E. B. Waizenegger, B. M. W. de Hepcée, G. L. Simpson, A. Valji and C. P. Berlinguette, *Joule*, 2024, **8**, 3106-3125.
18. H. Liu, H. Shin, X.-Y. Li, G. Su, P. Ou, Y. Wang, L. Chen, J. Yu, Y. Chen, R. Xia, G. Lee, K.-S. Lee, C. Yu, P. Wang, D. Choi, D. Zhou, C. Tian, I. Gereige, A. Alahmed, A.

Jamal, O. K. Farha, S. W. Boettcher, J. B. Dunn, K. Xie and E. H. Sargent, *Energy Environ. Sci.*, 2025, **18**, 6628-6640.
19. O. van der Heijden, S. Park, R. E. Vos, J. J. J. Eggebeen and M. T. M. Koper, *ACS Energy Lett.*, 2024, **9**, 1871-1879.
20. A. Y. Faid and S. Sunde, *Energy Technol.*, 2022, **10**, 2200506.
21. Y. Pan, Y. Li, C.-L. Dong, Y.-C. Huang, J. Wu, J. Shi, Y. Lu, M. Yang, S. Wang and Y. Zou, *Chem*, 2023, **9**, 963-977.
22. J. K. Nørskov, T. Bligaard, A. Logadottir, J. Kitchin, J. G. Chen, S. Pandelov and U. Stimming, *J. Electrochem. Soc.*, 2005, **152**, J23.
23. Y. Ren, W. Kong, Y. Li, W. Zhan, C. Zhang, Y. Miao, B. Yao, S. Li, Z. Li, X. Liu, S. Zhan, H. Zhou, M. Shao and H. Duan, *Nat. Catal.*, 2025, **8**, 771-783.
24. W. Lv, L. Pan, X. Zhang, C. Wang, M. Wei, R. Zhang, W. Wang and L. Wang, *Sci. China Mater.*, 2026.
25. Q. Liao, W. Li, Y. Wei and C. Han, *Chem. Commun.*, 2026.
26. W. Deng, P. Zhang, Y. Qiao, G. Kastlunger, N. Govindarajan, A. Xu, I. Chorkendorff, B. Seger and J. Gong, *Nat. Commun.*, 2024, **15**, 892.
27. J. Li, X. Chang, H. Zhang, A. S. Malkani, M.-j. Cheng, B. Xu and Q. Lu, *Nat. Commun.*, 2021, **12**, 3264.
28. S. Fukuzumi, Y.-M. Lee, H. S. Ahn and W. Nam, *Chemical Science*, 2018, **9**, 6017-6034.
29. L. An and R. Chen, *J. Power Sources.*, 2016, **320**, 127-139.
30. J. G. M. Winkelman, O. K. Voorwinde, M. Ottens, A. A. C. M. Beenackers and L. P. B. M. Janssen, *Chem. Eng. Sci.*, 2002, **57**, 4067-4076.
31. R. P. Bell and R. R. Robinson, *Trans. Faraday Soc.*, 1962, **58**, 2358-2359.
32. J. Newman, D. Bennion and C. W. Tobias, *Ber. Bunsenges. Phys. Chem.*, 1965, **69**, 608-612.
33. C. Espinoza, D. Kitto and J. Kamcev, *ACS Appl. Polym. Mater.*, 2023, **5**, 10324-10333.
34. A. Venkataraman, H. Song, V. D. Brandão, C. Ma, M. S. Casajus, C. A. Fernandez Otero, C. Sievers, M. C. Hatzell, S. S. Bhargava, S. S. Arora, C. Villa, S. Dhingra and S. Nair, *Nat. Chem. Eng.*, 2024, **1**, 710-723.
35. Z. Rastegar and A. Ghaemi, *Heat Mass Transf.*, 2022, **58**, 365-381.
36. G. T. Rochelle, *Science*, 2009, **325**, 1652-1654.
37. O. Gutiérrez-Sánchez, B. de Mot, N. Daems, M. Bulut, J. Vaes, D. Pant and T. Breugelmans, *Energy Fuels*, 2022, **36**, 13115-13123.
38. É. Hülber-Beyer, K. Bélafi-Bakó and N. Nemestóthy, *Chem. Pap.*, 2021, **75**, 5223-5234.
39. A. Hussain, H. Yan, N. Ul Afsar, C. Jiang, Y. Wang and T. Xu, *Front. Chem. Sci. Eng.*, 2022, **16**, 764-773.
40. J. S. J. Ferrer, S. Laborie, G. Durand and M. Rakib, *J. Membr. Sci.*, 2006, **280**, 509-516.
41. M. Yan, Y. Zhang, G. Zhu, X. Kong, T. Cang, D. Wang, H. Wibowo and E. Kanchanatip, *Environ. Sci. Pollut. Res.*, 2024, **31**, 35979-35991.
42. X. Zhu, P. Hao, Y. Shi, S. Li and N. Cai, *Adsorption*, 2020, **26**, 1227-1237.
43. G. Virruso, C. Cassaro, A. Culcasi, A. Cipollina, A. Tamburini, I. D. L. Bogle and G. D. M. Micale, *Desalination*, 2024, **583**, 117724.
44. L. Salas, A. Schwarz and A. Gonzalez-Vogel, *Environ. Sci.: Water Res. Technol.*, 2026, **12**, 588-600.
45. I. Group, *Formic Acid Prices, Trend, Chart, Demand, Market Analysis, News, Historical and Forecast Data Report 2026 Edition*, IMARC Group, 2026.

46. I. Group, *Formaldehyde Prices, Trend, Chart, Demand, Market Analysis, News, Historical and Forecast Data Report 2026 Edition*, IMARC Group, 2026.